Simulation of Large Earthquake Synchronization and Implications On North Anatolian Fault Zone

E. Sopacı[1], A. A. Özacar[2]

[1]Laboratoire Géoazur, Centre national de la recherche scientifique (CNRS), Sophia Antipolis, France
[2]Department of Geological Engineering, Faculty of Engineering, Middle East Technical University, Ankara, Turkey

Key Points:

- Afterslip propagation in barriers controls fault synchronization and predictability of large earthquakes.
- Asperity size is less significant, contradicting previous studies, implying that rupture styles influence long-term stress interaction.
- Static stress changes can lead to immature small ruptures, complex slip deficits, and failure times.
- Simulations can mimic the migrating earthquakes along NAF and suggest the Cinarcik segment as a possible barrier, disrupting the synchrony.

Corresponding author: Eyüp Sopaci, `sopaci@geoazur.unice.fr`

Abstract

The North Anatolian Fault (NAF) has a history of large quasi-static large earthquake clusters. This study investigates the phenomenon with a model consisting of three strong velocity-weakening (VW) asperities separated by velocity-strengthening VS barriers in a 2.5D model governed by rate-and-state friction. The results show that the after-slips at the VS barrier control the stress interaction and synchronization; hence, the barrier strength and size are the most important parameters. The static stress transfer can lead to immature ruptures that arrest within the VW asperity, adding complexity to failure times. The asperity size appears insignificant, challenging previous theories linking barrier efficiency to the asperity-barrier size ratios. Such discrepancy suggests that slip type, e.g., slip-pulse or crack-growth, influences the long-term failure time distribution. Even though the state evolution (aging and slip laws) for frictional strength within the RSF framework differ significantly in co-seismic ruptures, they resemble each other for after-slip propagation, highlighting the importance of after-slip propagation and adding robustness to our conclusions. The results from various simulation scenarios suggest that the after-slip extents and duration with the peak slip rates and rupture speeds are the indicators for the synchronization and the predictability of large earthquakes. Despite the simplicity of the governed model, the results can mimic the synchrony of large earthquakes along the NAF, which are disrupted by aseismic creep and complex fault geometries such as releasing bend (e.g., Cinarcik segment), step-overs (e.g., Niksar) and slip partitioning (Duzce-Bolu segments) acting as barriers.

Plain Language Summary

North Anatolian Fault Zone (NAF) shows quasi-periodic failures of large strike-slip earthquakes that resemble a super-cycle pattern within which the characteristic earthquakes fail sequentially in a close interval. However, the super-cycle pattern and quasi-periodic failures mostly relate to the mega-thrust fault zones. More interestingly, a west migrating pattern appeared clearer in the seventieth century, elevating the hope of large earthquake predictability. This study investigated the earthquake synchronization and triggering phenomena on a 2.5D continuum model with three strong vertical asperities separated by barriers. The fault interface obeys rate and state friction. Simulation results imply how the barrier structure and after-slip propagation control the synchronization process, mimicking NAF observations. The results also reasonably imply the possible extent of future earthquakes expected to fail at the observed slip deficit along the NAF.

1 Introduction

The North Anatolian Fault Zone (NAF) has a historical record of large earthquake clusters that characteristic quasi-periodic earthquakes fail sequentially within close time intervals (Şengör et al., 2005). The following earthquake generally nucleates close to where the former stops in the cluster, where those points correspond to the step-overs along the NAF shown in Figure 1 (Pondard et al., 2007). The observations suggest those step-over areas have remarkable stress and strength heterogeneity can be attributed to ”velocity-strengthening” barriers at the cluster edges, preventing ruptures from spreading from one segment to another or mitigating the transfer of stress (Kaneko et al., 2010; Lambert & Lapusta, 2021; Yıkılmaz et al., 2015; Cakir et al., 2014; Liu & Wang, 2023; Kondo et al., 2010; Kaya et al., 2009). In the recent situation, all segments of NAF from east to west have ruptured, except the locked segment(s) beneath the Marmara Sea, still building up strain for a large earthquake (Lange et al., 2019). This raises the question of what conditions synchronization happens and the large earthquakes become more predictable.

Studies of rock friction have established that a fault segment can undergo stick-slip motion if it is velocity weakening (VW) or tends to creep if it is velocity strength-

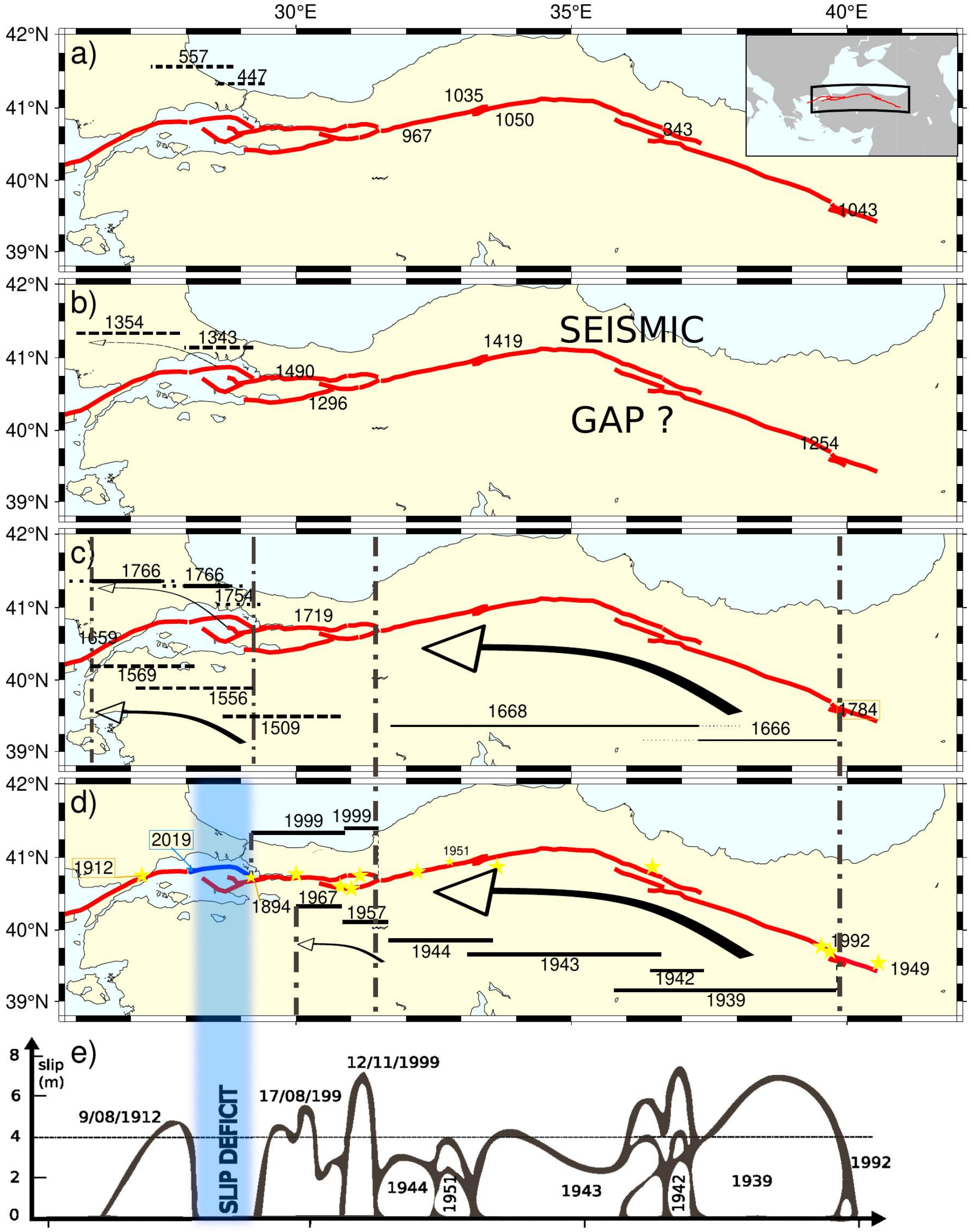
30°E
35°E
40°E
42°N
41°N
40°N
39°N
a)
557
447
1035
1050
967
343
1043
b)
1354
1343
1490
1296
1419
SEISMIC
GAP ?
1254
c)
1766
1766
1754
1719
1659
1569
1556
1509
1668
1666
1784
d)
2019
1912
1999
1999
1951
1894
1967
1957
1944
1943
1942
1939
1992
1949
e)
slip (m)
8
6
4
2
0
9/08/1912
SLIP DEFICIT
17/08/199
12/11/1999
1944
1951
1943
1942
1939
1992

Figure 1. Map showing the historical earthquakes along North Anatolian Fault zone (a-d) and synchronized clusters, and its approximate recent situation (e). The historical earthquake catalog is compiled from studies (Şengör et al., 2005; Bulut & Doğru, 2021; Pondard et al., 2007; Fraser et al., 2009; Parsons, 2004)

ening (VS) (Dieterich, 1979; Ruina, 1983). The type of motion is determined by the critical elastic stiffness relation within the framework of rate and state friction (RSF) in equation 1 (Ruina, 1983). If the stiffness is lower than the critical value $k < k_{cr}$, corresponding to the RSF parameter is $0 < a - b$, and the VW size is larger than a critical length (Ampuero & Rubin, 2008; Dieterich, 1992), the fault patch can nucleate earthquakes. The terms VW and VS patches refer to asperities and barriers, respectively.

$$k_{cr} = \sigma_n (b - a)/d_c \tag{1}$$

Numerical simulations assuming that the frictional stress on the fault is RSF have revealed various aspects of earthquakes and fault synchronization, including the asperity-barrier sizes, frictional properties, and relative distances between patches (Kato, 2004; Kaneko et al., 2010; Dublanchet et al., 2013; Cattania, 2019). The successive failure time delay between two VW patches embedded in VS medium increases as their separation distance increases (Kato, 2004). Simulation suggested that the VS barrier's effectiveness is related to the ratio between VW and VS sizes and the frictional properties of VS that control the probability of joint generation of a large earthquake (Kaneko et al., 2010). Also, the density of VW patches in a medium with the frictional properties of VS regions forms a threshold that determines the simultaneous failures of asperities and destabilization of the creeping region (Dublanchet et al., 2013). Moreover, the analog models investigated the synchronization patterns of mega-thrust earthquakes in nature, finding that the ratio of the barrier and asperity patches (Db/Da) determines the barrier's effectiveness (Corbi et al., 2017; Rosenau et al., 2019). Unlike the numerical simulations with RSF, Scholz (2010) argued that the synchrony of parallel faults necessitates similar intrinsic velocities to sustain a phase locking and classified the abutting fault synchronization into another category, likewise the pattern in NAF. However, Wei and Shi (2021) argued the role of the static stress transfer on fault synchronization by stating that static stress transfer leads to synchronization, unlike Scholz (2010). They also concluded that the barrier's width is more sensitive to synchronization than its frictional strength.

Our previous studies investigated the aftershock occurrence after the 30.10.2020 Samos Mw7.0 earthquake (Sopaci & Özacar, 2021) and the triggering potential of a moderate earthquake on the locked segments of the NAF, remaining from a large earthquake (Sopacı & Özacar, 2023) using spring slider system. Here, we explore the issue of long-term spontaneous segment failures using a numerical model designed to be analogous to the North Anatolian Fault (NAF). Our numerical setup includes three strong, vertically oriented VW asperities separated by VS barriers. We use the numerical method described by (Lapusta et al., 2000) with the spectral FFT code (Sopaci, 2022). Numerous simulations mimicked synchronized, complex, or independent classes of fault zones. Most simulations are generated by the quasi-dynamic (QD) method, simplifying the inertial effects via radiation damping to reduce numerical costs. Some QD results are compared with the full inertial effects on identical setups to avoid numerical artifacts (Thomas et al., 2014; Lambert & Lapusta, 2021). Similarly, identical setups run using aging and slip state evolution laws to account for the distinct frictional strength evolution on the interface (Dieterich, 1979; Ruina, 1983).

This study first checks if numerical simulations can generate large earthquake synchronization analogous to NAF. Since the recurrence intervals of characteristic earthquakes are generally long, there are a few well-documented ruptures with modern instrumentation. Therefore, this study intended to assist in understanding the synchrony of large earthquakes and earthquake-triggering mechanisms. The natural indicator of synchronized fault zones is investigated by generating synthetic earthquake catalogs with a controlled setup. The study also intends to examine the progressive synchrony behavior of NAF and its recent stress situation, where a large earthquake is expected (Şengör et al., 2005).

2 Simulation Set-up

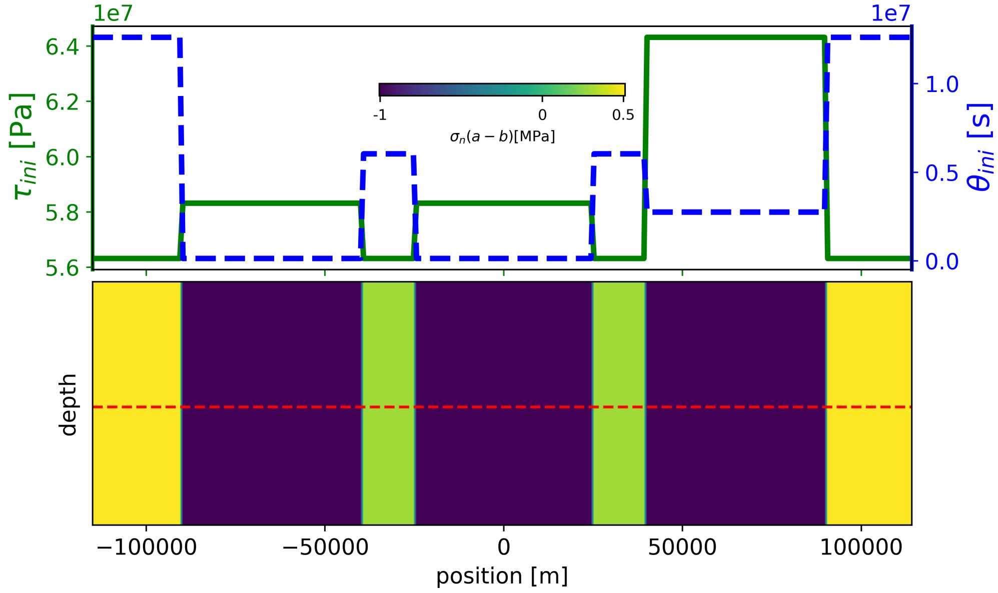

Figure 2. Simulation set-up: a) Initial values, b) a schematic representation of the fault in 2D medium.

We assumed three large asperities embedded in a 2D medium, where simulations correspond only to the red dashed line in Figure 2, and the width information is added with (Luo & Ampuero, 2018). The shear stress on the interface τ is assumed to be rate and state friction computed by:

$$\tau = \sigma_n \mu = \sigma_n \left[\mu_0 + aln\left(\frac{v}{v_0}\right) + bln\left(\frac{v_0\theta}{d_c}\right) \right] \tag{2}$$

where σ_n denotes the effective normal stress, μ and μ_0 are the friction and reference friction at the reference velocity v_0. The second and third terms on the right-hand side (2) contribute as velocity v (dynamic) and state θ (static) dependence of friction, where d_c is the critical slip distance. a and b are constitutive parameters for direct velocity and state evolution. Two empirical state evolution formulas for θ to complete equation 2, namely aging and slip laws, are given by (Dieterich, 1979; Ruina, 1983).

$$\dot{\theta} = 1 - \frac{v\theta}{d_c} \tag{3}$$

$$\dot{\theta} = -\frac{v\theta}{d_c} ln\left(\frac{v\theta}{d_c}\right) \tag{4}$$

The elastic stress is defined by:

$$\tau(x,t) = \tau^0(x) + f(x,t) - \frac{G}{2c_s}(v(x,t)) \tag{5}$$

where τ^0 is the loading stress, assuming no displacement discontinuity on the fault plane (Lapusta et al., 2000). The last term in equation 5, $G/2c_s(v(x,t))$ is the radiation damping to sustain a solution during rupture, where G and c_s are shear moduli, and speed (Rice, 1993). The second term is the stress transfer functional $f(x,t)$ due to the slip discontinuity, for which we applied the spectral FFT method Perrin et al. (1995); Lapusta et al. (2000):

$$\begin{aligned} \delta(x,t) - v_{PL}t &= \sum_{n=-N_{ele}/2}^{N_{ele}/2} D_n(t)e^{ik_nx} \\ f(x,t) &= \sum_{n=-N_{ele}/2}^{N_{ele}/2} F_n(t)e^{ik_nx} \\ k_n &= \frac{2\pi n}{\lambda} + \frac{2\pi}{W} \end{aligned} \tag{6}$$

where k_n is the spatial frequencies along the periodic domain λ and W is the width of the fault (depth) and N_{ele} is the number of elements over space domain. D_n and F_n are the complex Fourier coefficients of slip $\delta(x,t) - v_{PL}t$ and stress transfer functional $f(x,t)$, where v_{PL} is mean driving plate velocity. The Fourier coefficients of the stress transfer function are computed by:

$$F_n(t) = -\frac{G|k_n|}{2}D_n(t) + \int_0^{T_W} W(|k_n|c_st')\dot{D}_n(t-t')\,dt' \tag{7}$$

The first term is the so-called "static" term that contributes most during the slow phase. The second term contributes as the dynamic term, computed with truncated convolution integral within a window $(t_i, t_i - Tw)$ over coefficients history of $(dD_n(t)/dt)$ (Lapusta et al., 2000). In this study, we conducted most analyses by ignoring the second "dynamic" term for computational efficiency corresponding to QD approximation. We solved the equation of motion explicitly using Adams' multi-step predictor-corrector method by setting equations 2 and 5 equal and using a state evolution formula 3 or 4 (Hairer et al., 1993). We searched for synchronization patterns using the following simulation parameters.

Table 1. Simulation Parameters

Params	min	max	default
a_{asp}	0.005	0.015	0.01
$a_{bar} - b$	0.000	0.005	0.005
$d_c[mm]$	8	24	8
$L_{asp}[km]$	30	100	50
$L_{bar}[km]$	5	20	15

v_{PL}=0.02m/yr, G=30GPa, c_s=3km/s, μ_0=0.6
W=50km, σ_n=100MPa, $a_{asp} - b$=-0.01

As mentioned, the simulation outcomes obeying RSF depend drastically on the spatial resolution or length scales. We set the minimum number of cells per the cohesive zone to $\Lambda_0/dx \geq 9$ for $a_{asp} \geq 0.01$ and $\Lambda_0/dx \geq 12$ for $a_{asp} < 0.01$, where a_{asp} and dx denote minimum direct velocity effect parameter at the asperity and cell size. The cohesive zone is computed by:

$$\Lambda_0 = C_1 \frac{Gd_c}{b\sigma_n} \tag{8}$$

where C_1 is a constant around 1 (Erickson et al., 2020). The setting resolution according to equation 8 makes $h^*/dx \gtrapprox 20$ according to Lapusta et al. (2000), which is necessary to prevent cells from becoming unstable and failing independently where critical cell size h^* is computed by.

$$h^* = \frac{\pi}{4} \frac{Gd_c}{(b-a)\sigma_n} \tag{9}$$

3 Simulation Results

3.1 Classification of Results

We performed sensitivity analyses on parameters listed in Table 1 using initial conditions shown in Figure 2.

The fault zone is considered synchronized if all asperities fail sequentially within a close time. We first identify the failure times of full ruptures (a slip event covers the whole VW asperity). Then, we calculate the failure time difference between neighbor asperities during full ruptures and normalize them using the mean recurrence time for comparison. The status is set to synchronize if the normalized failure time differences converge to the value less than 10% percent of the mean recurrence time. For larger values, it is "independent," and the status is "complex" if failure time differences diverge.

The failure time differences of the synchronized fault zones are fitted to an exponential model $\beta_0 exp(\beta_1 x)$ as a function of its cycle count using the Gauss-Markov model with a constraint by forcing the model passes through the tangent line corresponding to the failure time difference between the successive events becomes stably short enough (it is converged to a value) (Koch, 1999). The fitting procedure allows a unique comparison by obtaining the synchronization rate and stability of the convergence. The fitted β_1 parameter represents the convergence rate (Schatzman & Schatzman, 2002). Let us now present examples of converged, complex, and independent cases.

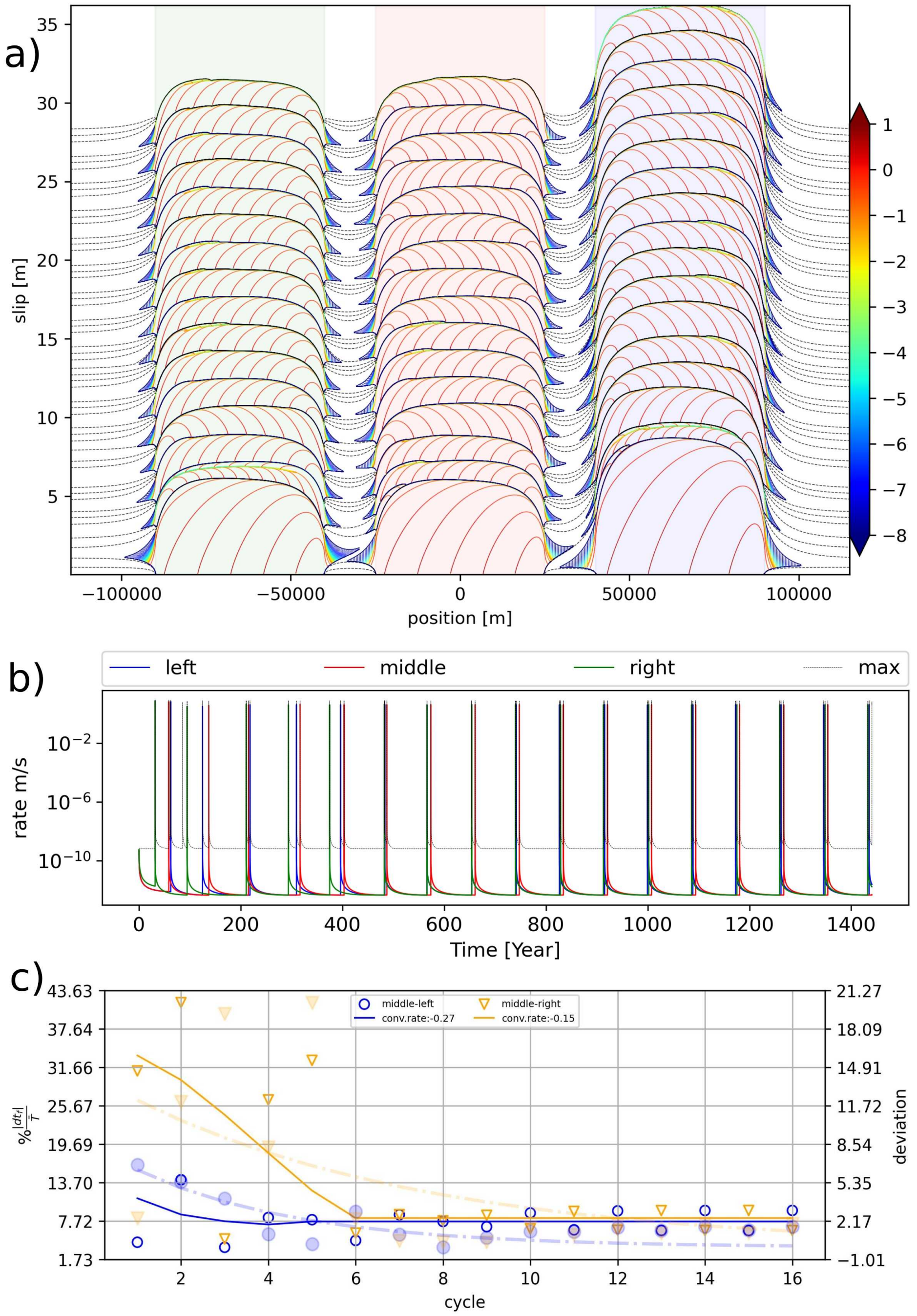

Figure 3. A synchronization example using slip law and default parameters in Table 1. a) slip profile: slip velocities are plotted in the logarithmic scale defined in the color bar on the right side. The dynamic rupture is plotted in two-second intervals, and post- or pre-seismic events are plotted with scatter plot until they reach a critical value $v_c = 10^{-8} m/s$. The inter-seismic times are plotted with black dashed lines every 20-year interval. b) time series of the middle of each asperity. The colors are given in the legend. c) Synchronization status of adjacent segments. Solid thin lines and scatters without face color denote constraint fit to normalized adjacent segment's failure time differences. The filled color scatters and bold dashed lines denote the deviations from the constraint fit.

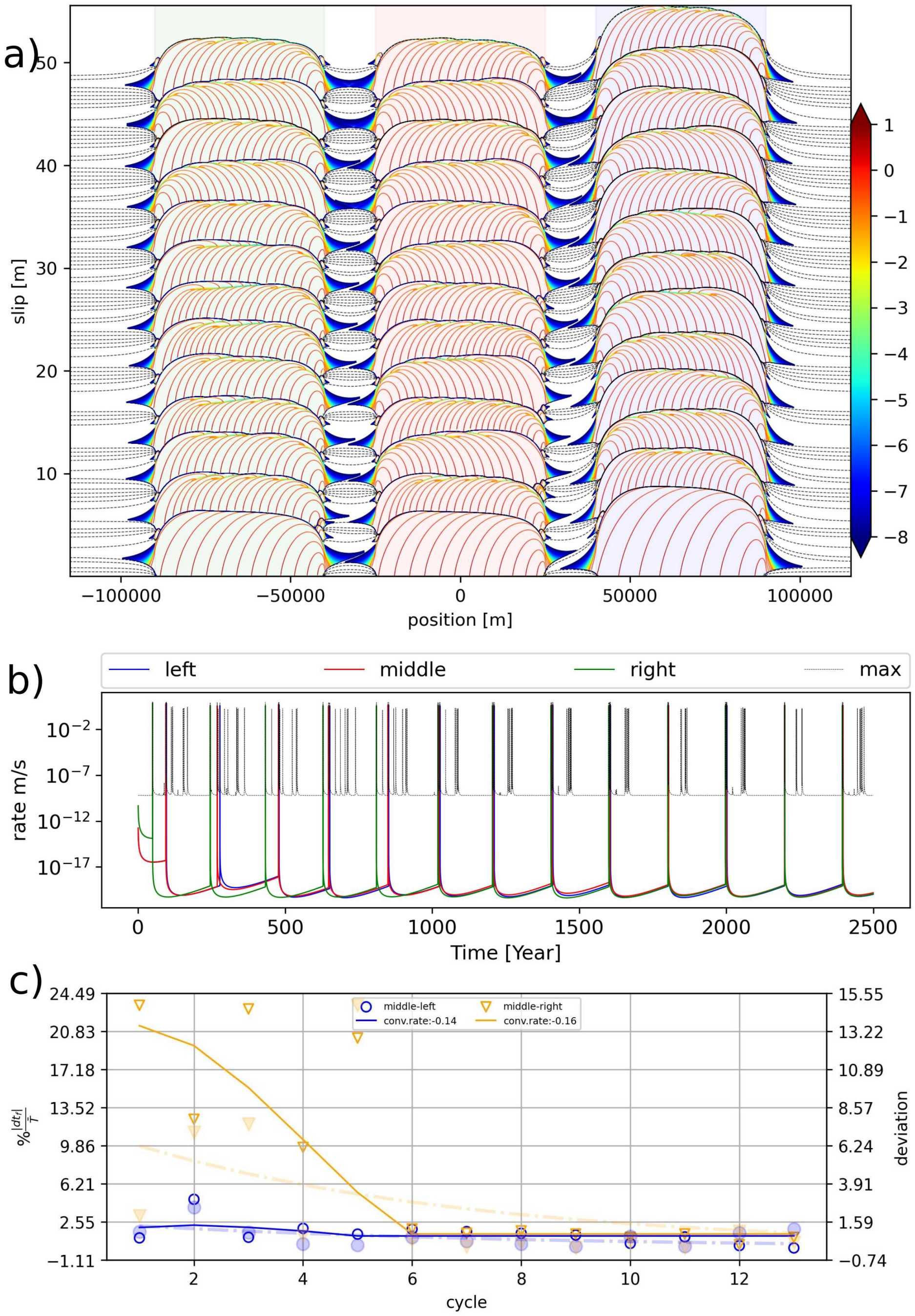

Figure 4. A synchronization example using aging law with default parameters in Table 1. a) slip profile: slip velocities are plotted in the logarithmic scale defined in the color bar on the right side. The dynamic rupture is plotted in two-second intervals, and post- or pre-seismic events are plotted with scatter plot until they reach a critical value $v_c = 10^{-8} m/s$. The inter-seismic times are plotted with black dashed lines every 20-year interval. b) time series of the middle of each asperity. The colors are given in the legend. c) Synchronization status of adjacent segments. Solid thin lines and scatters without face color denote constraint fit to normalized adjacent segment's failure time differences. The filled color scatters and bold dashed lines denote the deviations from the constraint fit.

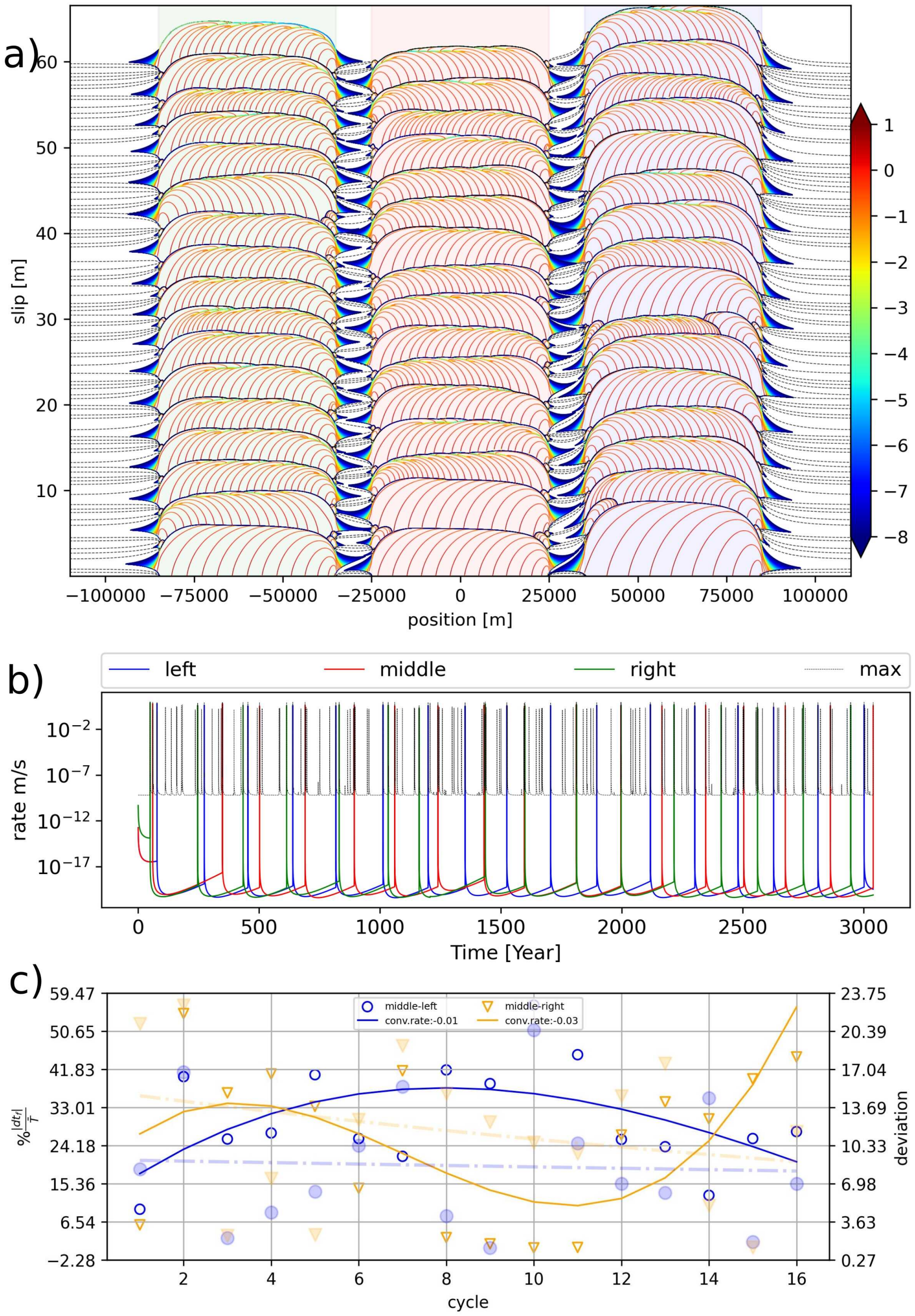

Figure 5. A complex example using aging law with default parameters in Table 1, except the barrier length decreased to 10km. a) slip profile: slip velocities are plotted in the logarithmic scale defined in the color bar on the right side. The dynamic rupture is plotted in two-second intervals, and post- or pre-seismic events are plotted with scatter plot until they reach a critical value $v_c = 10^{-8} m/s$. The inter-seismic times are plotted with black dashed lines every 20-year interval. b) time series of the middle of each asperity. The colors are given in the legend. c) Synchronization status of adjacent segments. Solid thin lines and scatters without face color denote constraint fit to normalized adjacent segment's failure time differences. The filled color scatters and bold dashed lines denote the deviations from the constraint fit.

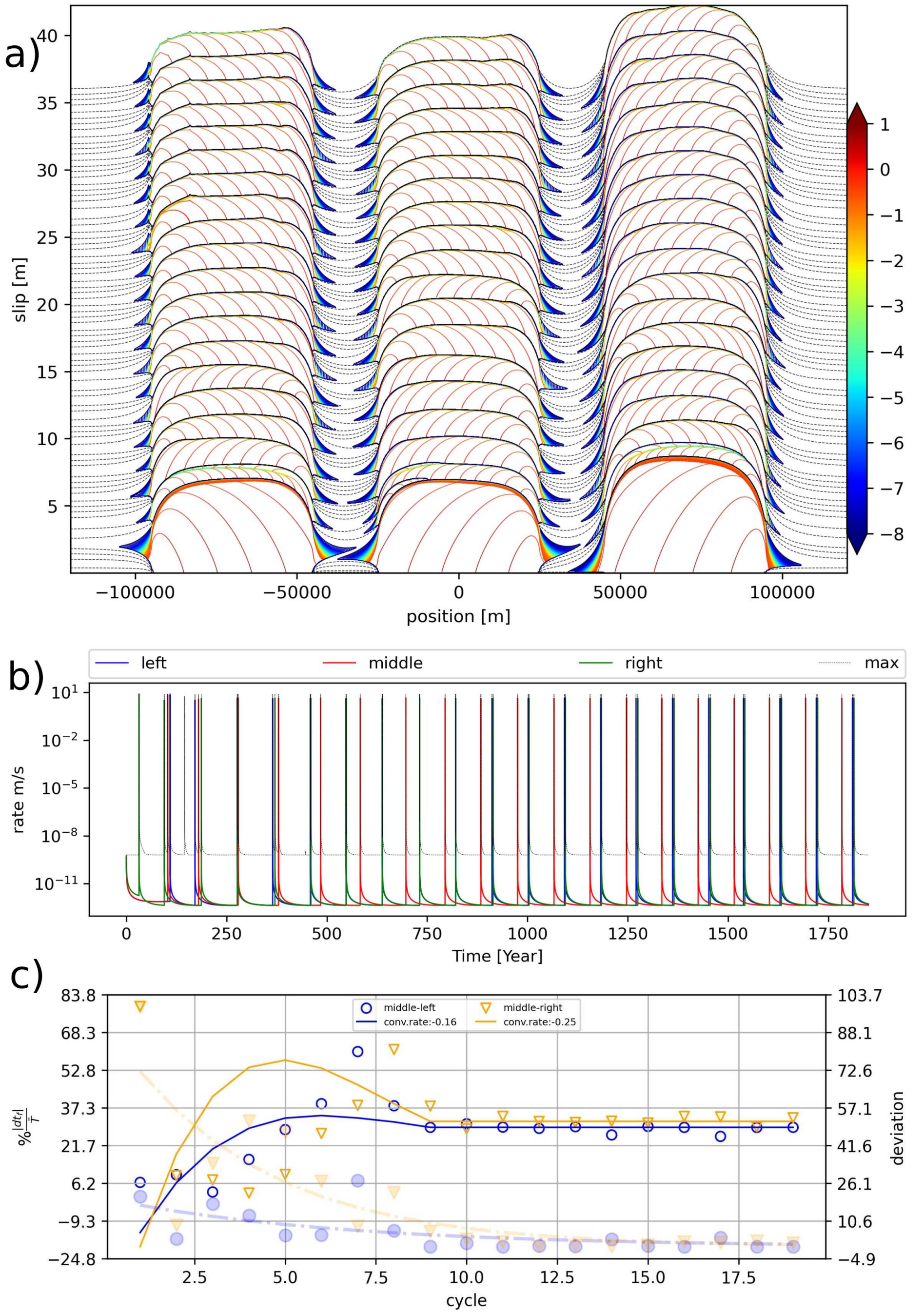

Figure 6. An independent status example using slip law with default parameters in Table 1, except the barrier length increased to 20 km and $a_{bar} - b = 0.003$. a) slip profile: slip velocities are plotted in the logarithmic scale defined in the color bar on the right side. The dynamic rupture is plotted in two-second intervals, and post- or pre-seismic events are plotted with scatter plot until they reach a critical value $v_c = 10^{-8} m/s$. The inter-seismic times are plotted with black dashed lines every 20-year interval. b) time series of the middle of each asperity. The colors are given in the legend. c) Synchronization status of adjacent segments. Solid thin lines and scatters without face color denote constraint fit to normalized adjacent segment's failure time differences. The filled color scatters and bold dashed lines denote the deviations from the constraint fit.

Figures 3 and 4 demonstrate a gradual decrease in failure time differences between neighboring asperities, leading to synchronization. Both setups have the same parameters, except different state laws govern the frictional interface. Although synchronization patterns are similar (as seen in Figures 3-b and c and 4-b and c), the dynamics of the state laws are vastly different. The wave speed of the slip law is twice as fast as the aging law (Figures 3-a and 4-a). The aging law sustains quasi-true stationary contact during slow loading with near-zero slip rates and twice the recurrence times and slip amounts per cycle compared to the slip law. The slip profiles (Figures 3-a and 4-a) also show that the slip extension and duration at the VS region is higher for the aging law. As we will see later, the aging law's generated peak stress is almost twice the slip law with the same setup. Still, due to higher fracture energy, the aging law can generate smaller events at the asperity edges by arresting the rupture within the VW region; the slip law tends to slip fully, exhibiting a vast difference in synchronization and triggering.

The studies previously stated that closer asperities and smaller barrier-asperity ratios mainly control synchronization processes (Kaneko et al., 2010; Corbi et al., 2017; Rosenau et al., 2019). However, the results in our simulations show otherwise that decreasing the barrier size from 15 km (Figure 4) to 10 km (Figure 5) leads to desynchronization of the fault zone. More variable-sized events emerge for closer asperities due to the triggering by the neighbor asperity, leading to immature events. These immature slips can not propagate fully, are arrested within the asperity, and leave stress further heterogeneity. On the other hand, weaker coupled asperities due to the longer barrier length and stronger velocity strengthening barriers sustain better synchronization. Still, too weakly-coupled asperities due to the barrier length (Figure 6) converge to a value higher than a threshold; they generate regular cycles but are classified as independent slip events.

3.2 Sensitivity Analyses

Figures 3 - 6 display how barrier length significantly changes the fault zone's synchronization pattern. Wei and Shi (2021) pointed out in a model with two asperities that the barrier's length is more important than its frictional properties. We examine the barrier's impact on synchronization by visualizing the barrier length change (with colors) and VS behavior ($a_{bar}-b$) change in different subplots in Figure 7. The extremely short (5km) and weak barrier ($a_{bar}-b < 0.003$) synchronizes very fast, regardless of the state law they govern. The slip law generally exhibits more regular cycles, either synchronized or independent failures. Yet, if the barrier is extremely weak $a_{bar} - b = 0.0$, it may generate complex earthquake cycles, as shown in Figure 7. The simulation with the aging law favors more partial ruptures; as a result, many simulations are classified as complex. On the other hand, it shows two distinct synchronization patterns depending on the barrier length and frictional strength. While the weak VS barrier ($a_{bar}-b < 0.003$) synchronizes very fast for short barrier lengths (blue color line in Figure 7), longer barriers require stronger VS $a_{bar} - b > 0.003$ so that neighbor events do not lead to triggered immature partial ruptures. For example, the 15 km barrier length with aging law (orange color at top subplots) can not synchronize unless the barrier is strong enough $a_{bar} - b = 0.005$ to inhibit the immature triggered rupture.

Figure 8 examines the parameters related to asperity. Decreasing the direct velocity effect parameter makes the asperity prone to triggering. For the aging law (Figure 8 upper-left subplot), all simulations display complex failure times as a_{asp} changes for the default barrier strength $a_{bar} - b = 0.003$. Inset Figure 8 (upper-left) for the aging law emphasizes how barriers' frictional properties significantly change the results; increasing barriers strength $a_{bar} - b = 0.005$ leads to synchronization of asperities. A similar pattern also emerges for the slip law (Figure 8 lower-left), showing the barrier's strength significantly affects the synchronization. While moderate barrier strength ($a_{bar} - b = 0.003$) exhibits synchronization for higher direct velocity effect parameter $a_a sp$, higher barrier strength in the inset $a_{bar} - b = 0.005$ leads to synchronization for lower $a_a sp$.

In other words, the asperity that is more prone to triggering synchronizes better with the strong barrier and vice-versa.

Subplots in the middle column of Figure 8 shows the effect of d_c on synchronization. According to the results for $d_c = 8 - 16mm$, no direct influence on synchronization is visible. We also tested $d_c = 24mm$, which can lead to bilateral rupture propagation due to increasing the nucleation zone (Dieterich, 1992; Ampuero & Rubin, 2008), but this does not change our conclusion on the synchronization. The asperity size is generally large enough to mimic the NAF's large strike-slip segments so that large earthquakes can nucleate at the VS-VW edge and fully slip. On the other hand, the larger d_c can change the post-slip slip pattern on the barrier, but it does not change our conclusion.

The change in the asperity size L_{asp} displays no significant influence on the synchronization pattern (right sub-figures 8). Our result on L_{asp} contradicts some studies relating the barrier efficiency to the asperity barrier length ratios (Kaneko et al., 2010; Corbi et al., 2017). One reason for such an exact opposite result is the rupture propagation type. Our model is specifically designed for the large strike-slip faults along NAF, with larger length-to-width ratio L_{asp}/W, so that slip generally nucleates at the one edge and slips over the domain with a self-healing pulse as observed from previous earthquakes (Konca et al., 2010). Therefore, we apply the $2.5D$ model (Luo & Ampuero, 2018), assuming that the slip averaged over the width. This assumption changes the rupture pattern to a self-healing pulse so that the slip does not grow as a crack-like pattern, leading to the maximum slip amount independent of the asperity length.

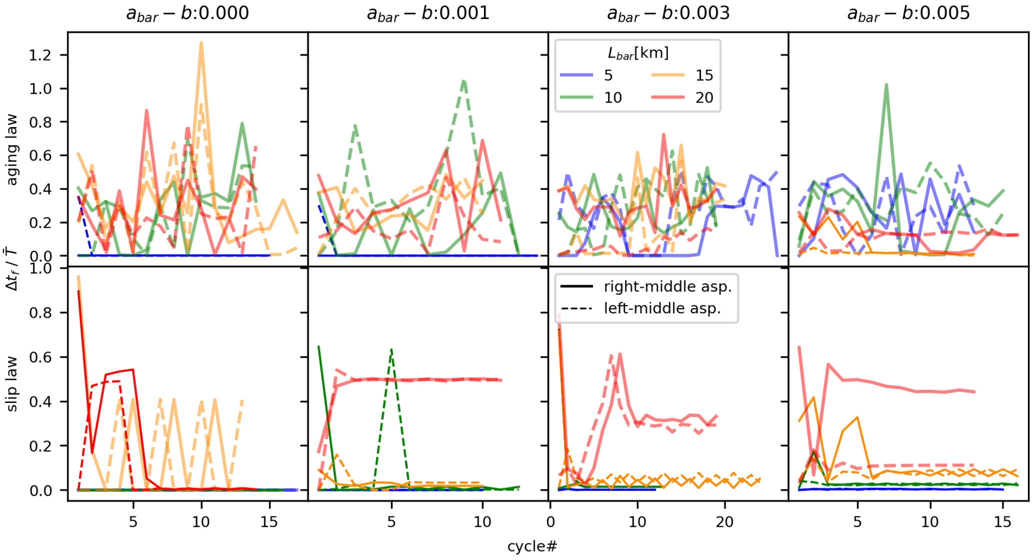

Figure 7. The figure shows the effects of barrier length and its frictional properties on synchronization. The horizontal and vertical axes are the earthquake cycle and the normalized (divided by the mean recurrence time) failure time differences between adjacent asperities. The effects of a change in the barrier's frictional properties ($a_{bar} - b$) and state types are plotted in vertical and horizontal orders, respectively. The failure time differences between right-middle and left-middle asperities are plotted with solid and dashed lines, and their colors indicate barrier lengths, given in the legends. he synchronized and complex setups are also distinguished by their line transparency to improve readability. Unless otherwise stated, the parameters are set to the default values in table 1.

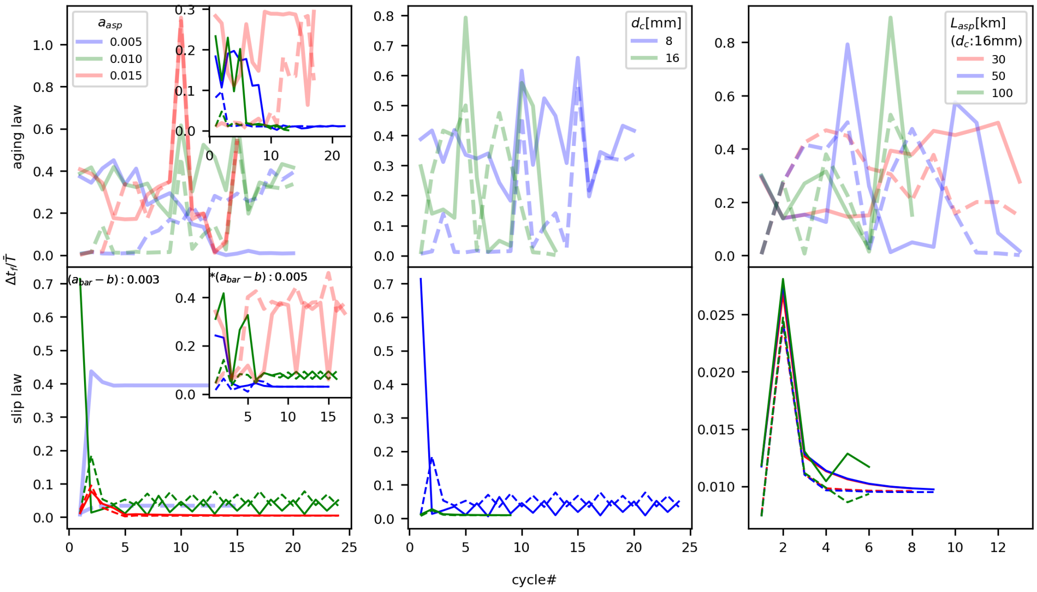

Figure 8. Figure shows the effects of asperity's frictional properties, size, and critical slip distance changes on the synchronization. The horizontal and vertical axes are the earthquake cycle and the normalized failure time differences between adjacent asperities. The effects of a change in the asperity's direct velocity effect parameter a_{asp}, critical slip distance d_c, and asperity length L_{asp} are plotted vertically for aging and state laws, respectively. The failure time differences between right-middle and left-middle asperities are plotted with solid and dashed lines. Changes in parameters are plotted with different colors, given in the legends. The synchronized and complex setups are also distinguished by their line transparency to improve readability. Also, in the inset figures, the barrier's frictional property is set to $a_{bar} - b = 0.005$ to visualize the effect of the barrier's strength. Unless otherwise stated, the default parameters are in table 1.

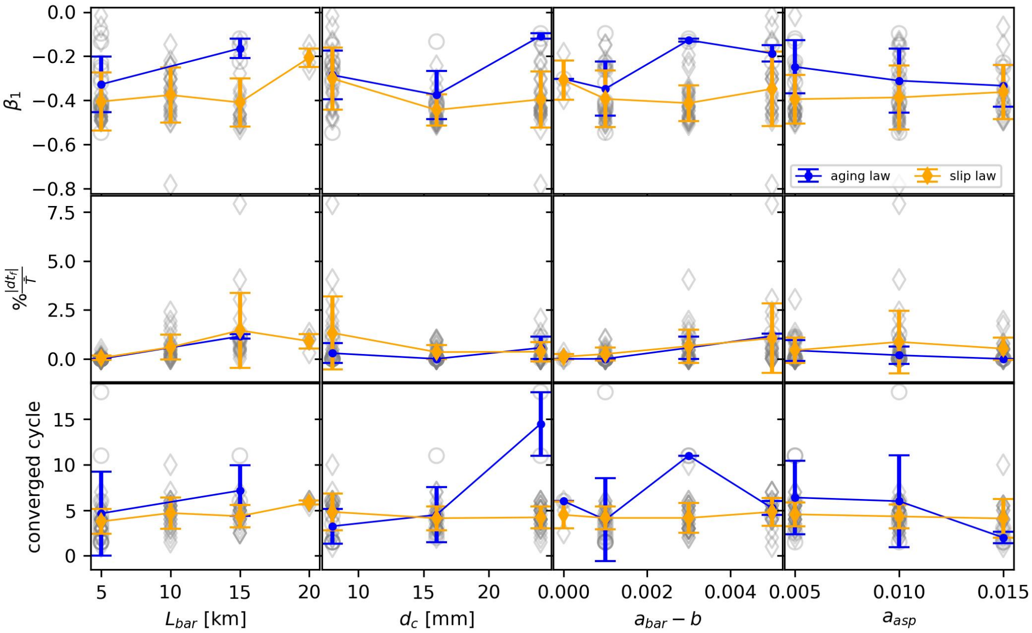

Figure 9. The plot shows how fast the faults are synchronized with changing certain parameters. The so-called convergence rates (β_1 of fitted deviance) are plotted on the top. The middle row shows the converged values, defined by the failure time differences in percentage between two successive large earthquakes of adjacent faults normalized by mean recurrence time. The lower row is the converged cycle defined, after which cycle faults synchronize.

Next, we order the convergences in Figure 9. The parameters that are sensitive to synchronization are grouped (the horizontal axes of Figure 9), and the results are compared for the β_1 parameter, the convergence value, and the converged cycle (the vertical axes of Figure 9). According to the exponential model, the convergence is faster and more stable for negative values of β_1 because it deviates less from the fitted model to residuals. The smaller converged value means the failure time difference is shorter, and lower converged cycles indicate a quicker synchronization. Figure 9 demonstrates that the slip law sustains a better synchronization than the aging law. The mean converged values (the difference between the full ruptures on the adjacent asperities) are similar for both laws unless the barrier is extremely large or strong ($L_{bar} = 20km$, $a_{bar} - b = 0.005$). The first column in Figure 9 demonstrates that lower barriers lead to faster synchronization, closer failure times, and higher deviations due to the strong coupling between asperities. Increasing critical slip $d_c = 8mm$ and $d_c = 16mm$ does not change the convergence, but a further increase to $d_c = 24mm$ leads to higher deviations. This deviation is not because d_c is a sensitive parameter to synchronization but because increasing d_c increases the nucleation half-length (Ampuero & Rubin, 2008) for nucleation of a slip event. For $d_c = 24mm$, slip events can nucleate closer to the asperity center rather than its VS-VW transition. The weaker barrier ($a_{bar}{-}b$) generally sustains better synchronization. The aging law shows a better synchronization for larger a_{asp}, which leads to a weaker triggering potential. On the other hand, the slip law shows less significance in its synchronization rate to the asperity's frictional because of its smaller fracture energy.

3.3 The role of static triggering

Figure 10 displays the five full rupture events on the middle asperity and their propagation over time. The state laws differ significantly during co-seismic ruptures but resemble each other in the post-seismic phase. The aging law's instantaneous stress increase on the barrier is twice the slip law's. Hence, the after-slip duration and peak slip values are larger, so the significant stress can reach the neighbor asperity for the aging law. If the barrier is short enough, the co-seismic rupture can propagate through the barrier and increase the stress level significantly at the asperity edge, so-called static stress triggering. Suppose the stress levels or slip deficits are close to each other. In that case, the rupture on one asperity can lead to another full rupture at the neighbor asperity, which we call synchronization. Otherwise, the static triggering leads to an immature event that can not fully rupture, generating further stress heterogeneity between the asperities. Here, the slip law is more inclined to synchronization because it can rupture with smaller fracture energy (Ampuero & Rubin, 2008). Even though two asperities have different slip deficits, an immature rupture can continue rupturing with smaller slip values, still able to equalize the stress balance.

To further emphasize our conclusion that static stress transfer leads to complex failures, the snapshots of slip propagation for complex and synchronized fault zones are shown in figure 11. Three successive slip events on the middle asperity and after-slips at the surrounding barriers are shown. The figure shows that three successive co-seismic rupture propagation are considerably similar, regardless of fault zone is synchronized or not. However, synchronized fault zones show remarkably smaller slip propagation, thus weaker triggering effects, justifying our conclusion that static stress transfer leads to complex failures.

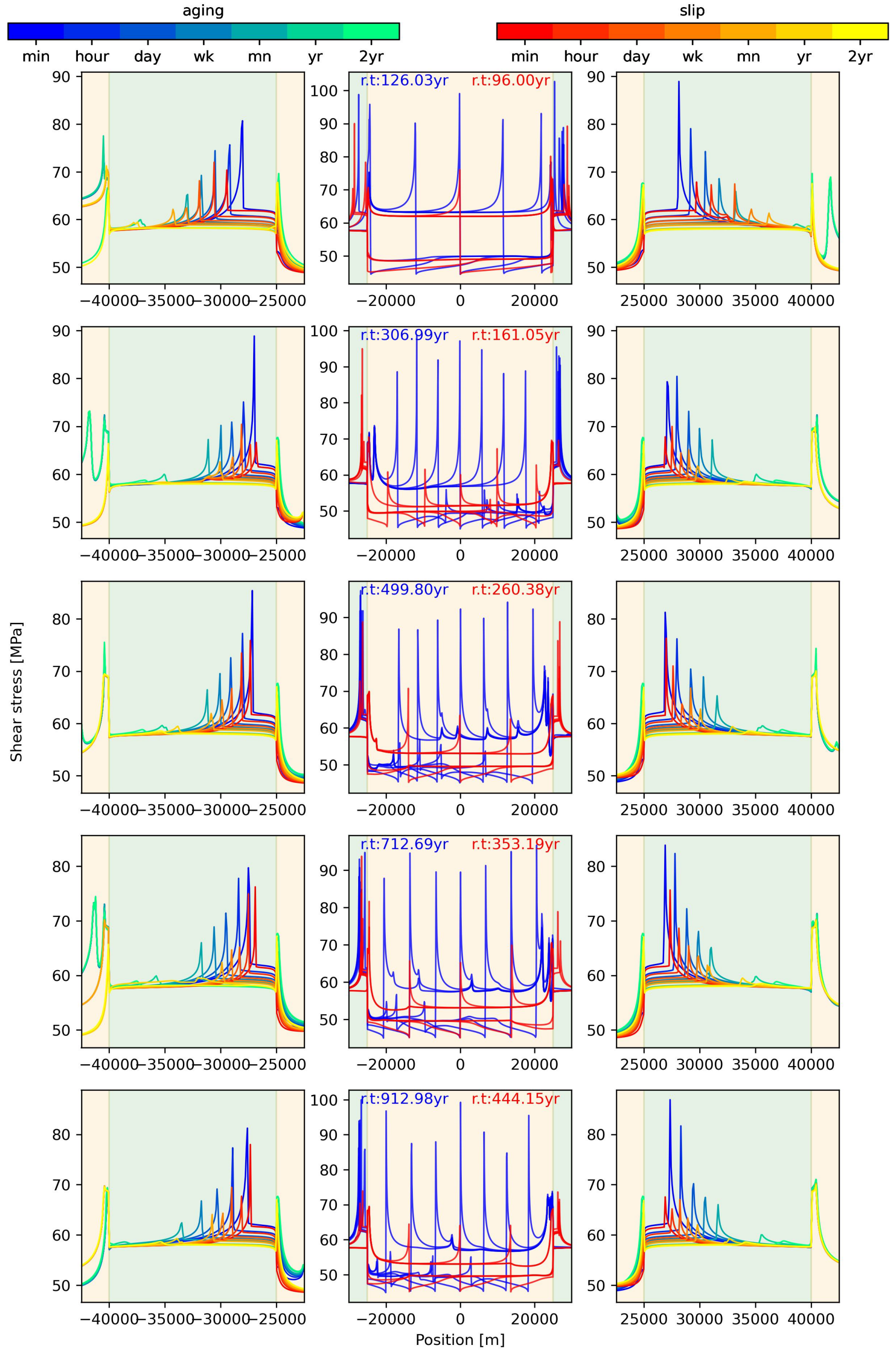

Figure 10. 5 full successive ruptures and post-seismic propagation of middle asperity are plotted. The default parameters in table 1 are used, except $a_{bar} - b = 0.003$. On the left and right, the propagation on the barrier is plotted with colored lines that define the time and state law, given in the color bar. The propagation on the middle asperity is plotted in the middle subplots with 5-second intervals. Rupture times are written in the middle plot for each state law with the color code defined in the color bar.

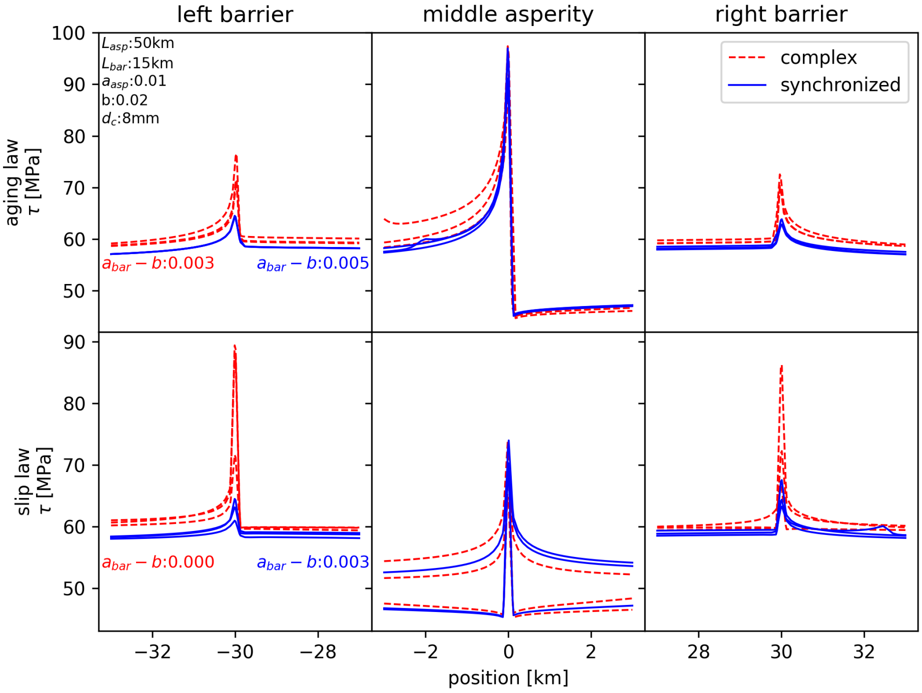

Figure 11. The stress propagation of complex and synchronized simulations are plotted for full ruptures on the middle asperity and continuation on the left and right barrier. The plotted waves correspond to the highest amplitudes of the first-fourth ruptures on the middle asperity and 5km away from it. The parameters for simulation are written on the first sub-plot (upper-left) and plotted with a color code for the synchronization status given in the legend. Complex and synchronized status simulations correspond to the $a_{bar} - b$ values given in the first column for aging and slip laws.

3.4 Indicator of synchronization and predictability of large earthquakes

Many scenarios generated synchronized, complex, and independent fault zones that can mimic characteristic earthquakes along major strike-slip fault zones like NAF. The simulation results show that the synchronized or independent fault zones exhibit higher velocities. Therefore, we plotted the clustered fault zones as peak velocities (PV) and concerning other observable in Figure 12. According to the results, fault zones with higher rupture lengths, shorter duration, and faster wave speeds are valuable indicators for large earthquakes' predictability. Besides, fault zones exhibiting shorter pre and post-seismic duration and length are more predictable. Also, the predictable earthquakes exhibit less co-seismic stress drop than the complex fault zones. On the other hand, the predictability is unrelated to the magnitude and maximum observed slip. The complex fault zones show a partial rupture ratio close to 1 (the rate between partial and full ruptures) due to the triggering of neighbor asperity, which leads to immature ruptures.

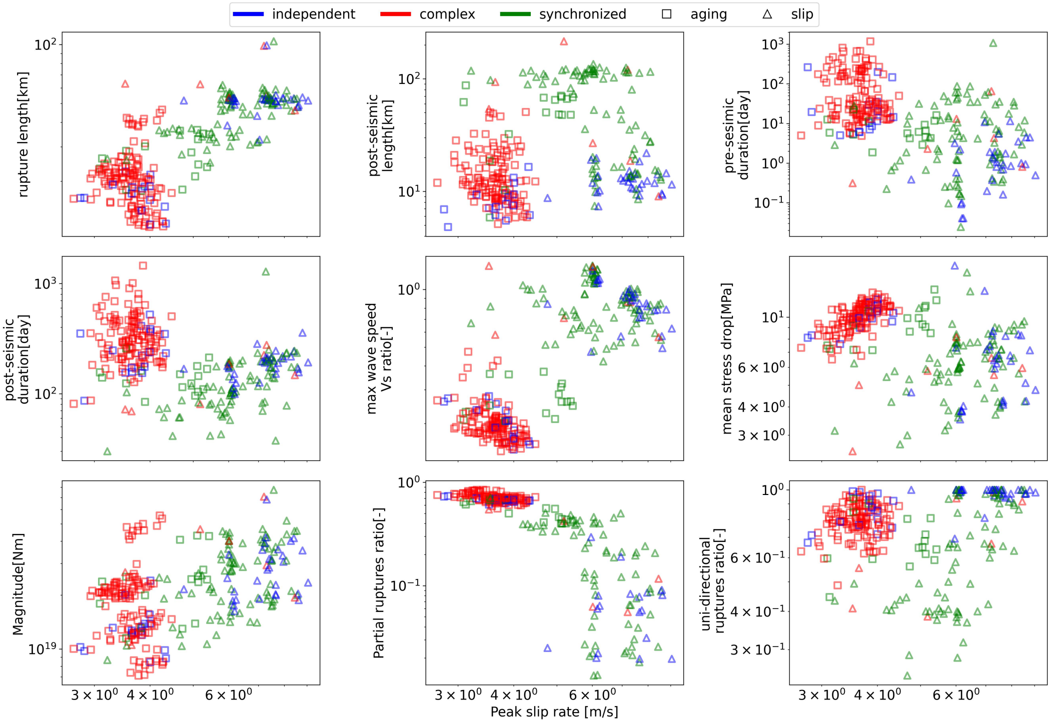

Figure 12. Peak Velocity (slip rate) [m/s] vs. Distribution stats of slip event

4 Discussion on results

We analyzed the spontaneous failure times of initially heterogeneous three vertical strong velocity weakening (VW) asperities separated by velocity strengthening (VS) barriers within the rate and state friction (RSF) framework. Our $2.5D$ numerical setup is designed for investigating the fault segments' synchrony along the North Anatolian Fault (NAF) Zone (Şengör et al., 2005). Still, the results will also shed light on other major fault zones. We extended previous studies using RSF (Wei et al., 2018; Shi et al., 2022) by considering different state laws, namely aging and slip laws (Dieterich, 1979; Ruina, 1983). The simplified inertial effect, the so-called quasi-dynamic (QD) method, was used in numerical simulations (Rice, 1993). Still, fully-dynamic (FD) effects with wave-mediated stress transfer were tested (Lapusta et al., 2000), in supplementary figures 1 and 2, which indicate despite the FD affects the co-seismic wave propagation significantly, FD has an insignificant effect on the synchronization. Therefore, we leave a detailed discussion on the FD effects on a later study.

We investigated the mechanisms of reciprocal earthquake triggering and synchronization. We applied analyses to determine fault synchronization's sensitive and insensitive parameters to reveal its possible mechanism. Examining the large data generated by the simulations led us to identify fault synchronization indicators that are observable in nature. This has important implications for understanding the predictability of large earthquakes, especially in major fault zones with limited reliable data like NAF due to long recurrence periods. Finally, this study aims to provide insights into the future seismic risks along NAF.

4.1 State laws

The simulation results reveal distinct dynamics for the aging and slip law. It is worth noting that the outcomes of numerical models with RSF depend on how well the grid points are resolved (Lambert & Lapusta, 2021). At least 9 or 12 grid points per the nucleation zone length Λ_0 are used (Equation 2) (Dieterich, 1992). The resolution is sufficient for the Aging law with the quasi-dynamic approximation (Lambert & Lapusta, 2021). Still, slip law requires denser grid points and necessitates indeed more computational resources (Ampuero & Rubin, 2008). However, we did not observe independently failing grids due to the coarse resolution with the slip law thanks to its weaker fracture energy, which tends to slip fully and thus reasonably generate robust solutions for the synchronization problem.

According to laboratory studies, aging law fails to fit large slip rates, while slip law performs better (Nakatani, 2001; Bhattacharya et al., 2015). Moreover, the Slip law promotes better transient triggering than the aging law due to its stronger weakening rate, but they show similar static triggering effects (Sopacı & Özacar, 2023). A significant divergence in the co-seismic dynamics emerges for both laws, but both laws resemble each other at the VS barrier (Figures 11, 10). Since we observed that the synchronization mechanism is mainly controlled by the barrier's strength or frictional properties, the choice of the state law did not change our conclusion. So, despite the differences between aging and slip laws, our observations regarding fault synchronization and the role of barrier properties remained consistent across the two state laws. This adds robustness to our conclusions and further supports the significance of barrier strength in fault synchronization dynamics.

4.2 Triggering and Synchronization

We observed two kinds of static triggering in our simulations. For the first kind, the coseismic slip can propagate through the VS zone to the neighbor VW asperity, or it nucleates within the VW zone but can not propagate and arrest within the VW zone, as a result changing the stress level in the vicinity (Gomberg et al., 1998). This happens if the barrier can not fully stop the afterslip propagation within its domain depending on the amount of load and, most importantly, its strength and size. Or the triggered immature event can not propagate future. The barrier can yield the loaded stress in the VS domain in the second static triggering mechanism, temporarily increasing the creep speed. The latter can lead to synchronization, while the first generally generated complex failure times in our results, unlike the results suggested by (Wei & Shi, 2021; Shi et al., 2022). These contradicting conclusions with similar studies can be due to their milder simulation setup, which shows how the rupture dynamics can drastically change the results. Figures 6 and 7 of (Wei & Shi, 2021) show the creep can penetrate through the asperity, and the earthquake nucleates close to the asperity center. Such creep penetration accounts for a setup in which the nucleation phase requires a larger slip directly related to d_c and a/b parameters, supposed that the seismogenic width is large enough (Cattania, 2019). In our simulation setup, the earthquakes generally nucleate at the asperity edges and propagate unilaterally as a self-healing pulse along the VW asperity, diverging from their dynamics. More to the point, such large nucleation zones with the higher d_c were discussed as non-physical (Rubin & Ampuero, 2005); since then, the nucleation process should have been detectable from the earth's surface. Therefore, we suggest static triggering leads to asynchronous failure times, justifying (Scholz, 2010).

Through temporary changes in stress due to waves passing by and under certain conditions, the external perturbations can lead to a self-acceleration of the locked patch (Sopacı & Özacar, 2023). The slip law's sensitivity to an external perturbation is higher than the aging law's due to its stronger weakening term (Nakatani, 2001; Sopacı, 2023). Nonetheless, the static triggering effects are several times higher than the transient effects (Sopacı & Özacar, 2023). Since the simulations started with initially heterogeneous stress, we do not think the transient effects are responsible for driving the segments into synchrony; instead, it is the afterslip propagation.

4.3 Sensitive parameters

Our results suggest strong barriers can dampen the after-slip propagation; as a result, the stress transfer occurs aseismically and sustains synchronization, whereas weak barriers allow triggered immature small events and lead to more variable-sized and complex failure distribution. The $\sigma_n(a-b)$ parameter of the barrier mainly controls the barrier's strength. The length of the barrier is not directly related to the barrier's strength, but the longer it is, the less the coseismic slips can reach the neighbor barrier and lead to immature earthquakes. More to the point, the inset subplots in figure 8 show how changing the barrier's strength changes the synchronization dependence on other parameters. In that sense, our sensitivity analyses diverge from the (Wei & Shi, 2021), stating that the barrier's length is more important than its frictional properties.

The simulation results in this study show that the synchronization depends ambiguously on the asperity parameters. The numerical earthquake triggering studies with RSF state that the direct velocity effect parameter controls the response to an external perturbation; thus, the smaller a_{asp}, the more prone it is to be triggered. Sensitivity to a_{asp} in figure 8 shows how asperity that is prone to triggering $a_{asp} = 0.005$ can synchronize for strong barrier $b - a_{bar} = 0.005$ but shows complex failure with $b - a_{bar} = 0.003$. Figure 8 also shows that the change in the asperity size shows insensitivity to synchronization. Our conclusion contradicts the idea that the asperity barrier ratio quantifies the barrier efficiency and controls the asperity synchronization process (Corbi et al., 2017; Kaneko et al., 2010). In this study, the three asperities with identical properties dictate pulse-like ruptures that unilaterally propagate along the strike, assuming the slip is the same within a finite width W (Luo & Ampuero, 2018). The rupture styles, such as crack-like growth or slip pulses, can change the recurrence patterns from chaotic to quasi-periodic (Nie & Barbot, 2022). Also, the 3D complex fault structure may lead to more complex failure sequences closer to statistical power laws in nature (Yin et al., 2023), thus may show more sensitivity to asperity properties. However, our main conclusion states that the barrier strength mainly controls the synchronization, and thus, the predictability of earthquakes would not change.

Moreover, critical slip distance d_c is used several times larger than the laboratory experiments for the sake of the computational burdens (Ampuero & Rubin, 2008; Lapusta et al., 2000). The value of d_c also dictates the minimum nucleation length scales to generate seismic events (Dieterich, 1992; Rubin & Ampuero, 2005; Ampuero & Rubin, 2008). The values used in this study for d_c do not alter the synchronization results. However, different rupture styles emerge for the upper values of d_c, also affected by the constitutive parameters a and b, and effective normal stress, which can impact the complex failure time occurrences (Cattania, 2019), should be noted.

4.4 Predictability Of Large Earthquakes

Synthetic data generated by numerous scenarios fitting the NAF analogy reveal that the predictability of fault zones is correlated to the peak slip rate, after-slip propagation, and rupture speed. Predictable synchronized earthquakes generally exhibit relatively long silent periods and successive full ruptures resembling super-cycles. Super-cycles are generally associated with subduction zones and thrust faults, showing quasi-periodic recurrence intervals (Herrendörfer et al., 2015; Salditch et al., 2020). Even though not quite similar and quasi-regularly compared to subduction zones, the strike-slip fault zones show clustered and synchronized segments in time and space as observed along NAF (Şengör et al., 2005; Bouchon et al., 2021). The mature fault zones are generally less likely to produce smaller events and host pulse-like earthquake ruptures that can propagate throughout the seismogenic zone (Thakur & Huang, 2021; Lambert et al., 2021). Even though it has not been well established, the rupture speed and rupture type, i.e., crack growth or slip pulse, are interrelated (Huang & Ampuero, 2011). The synchronized fault zones in this study slip fully with faster propagation speed and higher peak slip rates, suggesting mature fault zones are likely to synchronize. Also, our results justify the importance of slow aseismic slip as a mechanism of large earthquake nucleation and triggering (Nie & Barbot, 2022; Bouchon et al., 2021; Nalbant et al., 2023). Identifying the creeping regions and tracking the aseismic motion are the keys to identifying future seismic risks.

5 Implications On North Anatolian Fault Zone

North Anatolian Fault Zone (NAF) is one of the most active strike-slip fault zones. The fault segments fail quasi-periodically with approximately 250-300 years of recurrence interval, exhibiting a super-cycle-like pattern; large earthquakes fail relatively quickly and proceed with a long seismic quiescence. This sequential failure pattern constitutes clusters, and discreteness appears between the clusters due to the failure time differences (Bulut & Doğru, 2021). The synchronized clusters became more regular after the seventeenth century, which was less clear before (Şengör et al., 2005). In the twentieth century, a new sequence of large earthquakes began with the MS7.9 Erzincan (1939) at the eastern edge of the NAF. It migrated towards the west following MS7.1 Niksar-Erba (1942), MS7.5-7.7 Tosya-Ladik (1943), MS7.4 Bolu-Gerede (1944) ruptures (Şengör et al., 2005) (see also Figure 1). Remarkably, the following earthquake nucleated near where the preceding rupture stopped. The synchronization slowed down after the Bolu-Gerede segment, where the NAF splits into two branches: the north branch that dives into the Marmara Sea, called the Main Marmara Fault Zone (MMF), and the south branch (Bulut & Doğru, 2021). The sequence continued with the 1955 and 1967 earthquakes along the southern branch, while the northern branch waited 55 years until the Mw7.6 Izmit rupture on 17.08.1999. Three months later, on 12.11.1999 Mw7.2 Duzce fault ruptured at the eastern edge of the Izmit rupture. This earthquake doublet was an example of a delayed triggering, explained mostly by the conventional static stress transfer (Stein et al., 1997). The MMF segment lies on the western side of the Izmit segment, which is thought to be the last chain to complete the 1500 km-long cycle. Kumburgaz and Cinarcik subsegments within MMF remain unbroken in this current situation and have been most likely loading for a $M > 7$ earthquake (Lange et al., 2019).

The static stress transfer computations can reasonably indicate the elevated stress buildups but can not fully explain further triggering. For example, the Mw7.2 Duzce (12.11.1999) event does not correlate the mapped stress distribution with the previous events; instead, the maximum slip corresponds to the stress shadow of two adjacent M7.4 (1944, Bolu-Gerede) and Mw7.6 (1999, Izmit) ruptures and the hypocenter stands at the stress neutral region $\Delta\tau \approx 0$ (King et al., 2001; Utkucu et al., 2003). The stress and frictional state heterogeneity and the effect of an an-elastic time-dependent process during the nucleation are proposed to explain this inconsistency (Bouchon et al., 2021; Lorenzo-Martín et al., 2006; Pucci et al., 2007). Further, the Duzce rupture plane shows distinctly higher electric resistivity for the eastern where high slip occurred but had the stress shadow from previous ruptures. In contrast, the western part closer to the Mw7.6 Izmit rupture showing high-stress load has remarkably weaker resistance, interpreted as possibly a circulation of hydro-thermal fluids (Kaya et al., 2009). Supporting the idea, the lower normal stress in the western part is proposed to inhibit the Izmit rupture propagation as a barrier and lead to the three-month delayed triggering (Pucci et al., 2007). Suppose faults consist of VW asperities embedded in a VS barrier-like environment. In that case, co-seismic slip can jump from one asperity to the other, mainly controlled by the VS environment, as an alternative view to geometric complexity (Kaneko et al., 2010). Therefore, we argue that frictional stress heterogeneity and after-slip propagation at the western part of the Duzce fault better explain the inconsistency of the static stress transfer.

The trench observations also suggest the Bolu-Gerede segment (1944, east to the Duzce segment) consists of multiple asperities. These asperities failed synchronously, at least for the previous four ruptures, generating regular quasi-periodic cycles with similar sizes (Kondo et al., 2010). Furthermore, recent INSAR observations suggest that five creeping segments along NAF correlate well with the nucleation and arrest of large earthquakes (Liu & Wang, 2023). They are Izmit, Ismetpasa, and Destek creeping segments, which were also reported previously (Cakir et al., 2014), and two newly identified creeping segments: in the middle of the 1939 earthquake and the spatial gap between the 1939 and Ms 6.8 Erzincan (1992) rupture to the east. Combined with the step-overs, these regions perhaps control the synchronized earthquakes along NAF. Let us investigate three remarkable possible barriers and discuss their roles.

The Izmit segment was the final destination of the earthquake sequences, and recent observations suggest the western part of the Izmit segment is still creeping (Aslan et al., 2019). Besides, the 30 km Cinarcik releasing bend forms a depression that separates the Izmit and Kumburgaz strike-slip segments, generating a large zone of ($\sim$ 14 km thick) fault complexity (Armijo et al., 2005; Pondard et al., 2007; Uçarkuş et al., 2011). According to our numerical simulations, barriers over 20km long generally prevent significant stress transfer, leading to more independent failures. This may provide a basis that two strike-slip fault segments (Izmit and Kumburgaz) did not fail synchronously due to the Cinarcik releasing bend acting as a barrier.

A small break of the Cinarcik segment with normal fault mechanism is probably correlated to the MS6.3 1963 event, while larger M$\sim$7 1894 is to the southern branch of NAF in Marmara according to the sea floor investigation (Armijo et al., 2005). Therefore, the Cinarcik segment can be considered overdue; the last rupture beneath Marmara, possibly including the Cinarcik segment, was either in 1766 or 1754 (Pondard et al., 2007).

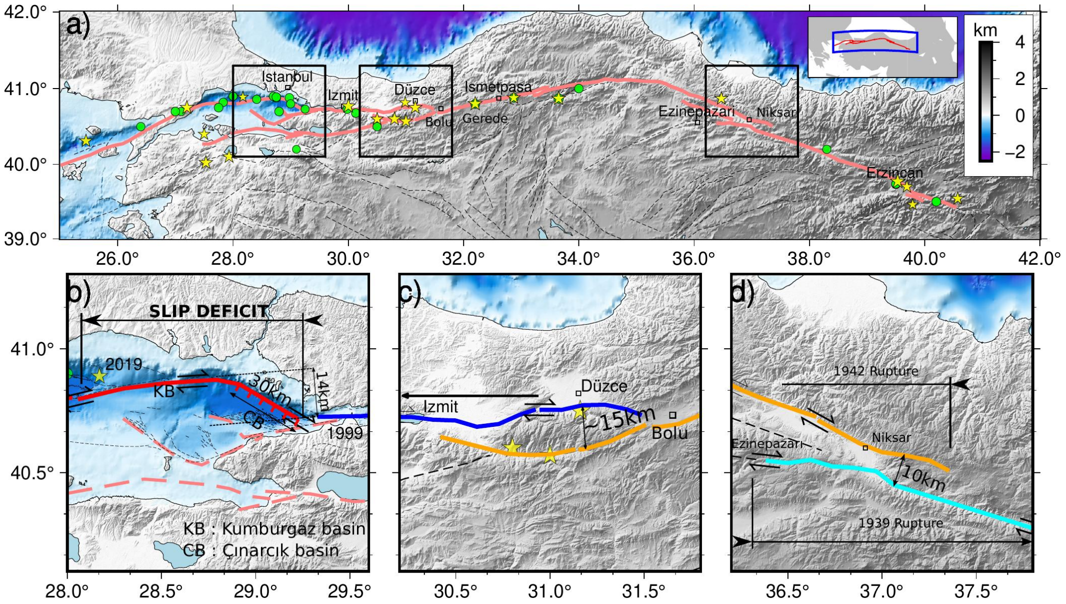
a)
42.0°
41.0°
40.0°
39.0°
26.0°
28.0°
30.0°
32.0°
34.0°
36.0°
38.0°
40.0°
42.0°
Istanbul
Izmit
Düzce
Bolu
Ismetpasa
Gerede
Ezinepazari
Niksar
Erzincan
km
4
2
0
−2
b)
SLIP DEFICIT
2019
KB
30km
CB
14km
1999
KB : Kumburgaz basin
CB : Çınarcık basin
41.0°
40.5°
28.0°
28.5°
29.0°
29.5°
c)
Izmit
Düzce
~15km
Bolu
30.5°
31.0°
31.5°
d)
1942 Rupture
Niksar
Ezinepazari
10km
1939 Rupture
36.5°
37.0°
37.5°

Figure 13. The Map (a) shows the synchronized segments along NAF in different color codes. The segment boundaries are highlighted with a black frame on map (a) and plotted on a larger scale in b-d.

However, there is still no satisfying proof during which earthquake the Cinarcik segment ruptured. On the western side, the Mw7.4 1912 Ganos earthquake is suggested to continue to the Central Marmara basin and stop similar to the Izmit earthquake that stopped at the Cinarcik releasing bend (Aksoy et al., 2010). In this respect, Kumburgaz and Cinarcik segments display slip deficits that can rupture during the next earthquake (Lange et al., 2019).

Recently, a moderate earthquake (Mw5.9 29.09.2019) occurred along a secondary fault near the Central Marmara Basin at the western tip of the Kumburgaz segment. It sparked a debate about whether it could trigger the expected large Marmara earthquake (Karabulut et al., 2021). According to our numerical investigations, the moderate event was not strong enough to trigger a large earthquake however, it could potentially advance the failure time (Sopacı & Özacar, 2023). However, the most important question still remains: where will the next earthquake nucleate, and what will be its extent?

According to our results, the two adjacent segments act as synchronized for a few cycles due to triggering and stress interaction, but this synchronization can be temporary (Figures 7 and 8). This result suggests that a failure of Kumburgaz and Cinarcik segments in one single earthquake is possible if two segments are considered overdue (Bohnhoff et al., 2013; Lange et al., 2019). In that scenario, once an earthquake is nucleated within the Kumburgaz or Cinarcik segment, wave propagation can trigger the other earthquake instantaneously (Sopacı & Özacar, 2023). On the other hand, two large segments can fail with a delayed time, possibly similar to 1776 and 1754 events (Parsons, 2004; Pondard et al., 2007). The Cinarcik segment is likely weaker with a shorter recurrence interval due to active normal faulting in comparison to the adjacent strike-slip segments (Kumburgaz and Izmit), which complicates the long-term failure times of NAF and is one of the main reasons why synchronization slows down (Bulut & Doğru, 2021).

Historical earthquakes exhibit the west migrating synchronization rate slowed down after the Bolu segment (1944 rupture) (Bulut & Doğru, 2021), where NAF splits into north and south branches constituting a 10-15 kilometer width step-over with remarkable stress transfer appeared to be between the branches (Lettis, 2003). According to our results, the stress transfer in such distances can affect the synchronization depending on the barrier's frictional properties. Many of our results suggest that the static stress transfer breaks the synchronization pattern due to leading immature earthquakes. More to the point, the difference in the slip distribution of the Duzce (Mw7.2, 12.111999) rupture can originate from the mechanical interaction between the Duzce and Izmit segments joint (Pucci et al., 2007), further complicating the failure times.

The MS7.8 Erzincan (1939) earthquake started a series of large earthquakes (1942, 1943, 1944), nucleated at the eastern edge of the Erzincan fault, and propagated unilaterally approximately 250 km to the west. Instead of following the main path of NAF, it propagated along the Ezine Pazari fault, the southern branch of the Niksar pull-apart region, about 75 km (Cakir et al., 2014). The observed slip values were comparably low at the Niksar pull-apart region, and possibly, it acted as a barrier (Cakir et al., 2014; Zabci et al., 2011). However, the previous 1668 earthquake MS 8 is thought to have broken the whole segments, jumping over the 10km length step over including the Erzincan fault (1939-1944 ruptures in the twentieth century) after a large seismic gap, (Şengör et al., 2005). The recent cycle did not break the whole segments as in the seventieth century and broke sequentially was explained by the rupture propagation driven by the geometrical frictional differences (Cakir et al., 2014). In 1939, once the rupture could not jump the 10 km length step over due to the higher stress level along the Ezine Pazari, it led to a stress shadow onto the Erbaa-Niksar segment, leading to 3 years of delay. Therefore, it can lead to a larger earthquake as in 1668 for the next cycle (Cakir et al., 2014), showing the significance of the barrier's frictional and geometric structures for the seismic risk assessments.

6 Conclusion

Motivated by the synchronized historical pattern along the North Anatolian Fault (NAF) Zone, we investigated the fault synchronization on a 2.5D physics-based asperity-barrier model in the rate and state friction (RSF) framework. The simulations started with initially heterogeneous conditions, and after several spontaneous ruptures with various scenarios, we investigated the conditions that the fault zone can adequately equalize the stress levels between the segments, leading to synchronization. Results reveal that static stress transfer can lead to immature triggered events, so the slip deficit or stress heterogeneity remains, leading to complex failure times. On the other hand, the strength and size of the aseismic zones control the synchronization process. Thus, determining the aseismic zones and examining their slow and silent dynamics have the uppermost importance for the predictability of large events. The asperity size did not show significance in synchronization in our study. However, it should be noted that the rupture style affects long-term synchronization patterns, which depend on the constitutive RSF parameters and the asperity size relative to nucleation length scales within the RSF framework. The different rupturing styles can account for why similar studies suggested that the barrier efficiency depends on the asperity size, while we suggested the opposite. Our simulation setup fits the mature fault zone with characteristic and quasi-periodic failures along earthquakes that nucleate at the transition zones and rupture unilaterally as slip-pulses, mimicking NAF. Even though the simulation setup is too simple for NAF, the results can explain the synchronized clusters along it, where the synchronization rates slow down, and where they behave independently.

Open Research

No data were used nor created in this study. The code is publicly available in GitHub-Zenodo (Sopaci, 2022). The maps are generated using GMT 6.0 (Wessel et al., 2019).

Acknowledgments

The numerical calculations reported in this paper were fully/partially performed at TUBITAK ULAKBIM, High Performance and Grid Computing Center (TRUBA resources).

References

Aksoy, M. E., Meghraoui, M., Vallée, M., & Çakır, Z. (2010). Rupture characteristics of the ad 1912 mürefte (ganos) earthquake segment of the north anatolian fault (western turkey). *Geology*, *38*(11), 991–994.

Ampuero, J. P., & Rubin, A. M. (2008). Earthquake nucleation on rate and state faults - Aging and slip laws. *Journal of Geophysical Research: Solid Earth*, *113*(1), 1–21. doi: 10.1029/2007JB005082

Armijo, R., Pondard, N., Meyer, B., Ucarkus, G., Lépinay, B. M. D., Malavieille, J., … Sarikavak, K. (2005, 6). Submarine fault scarps in the sea of marmara pull-apart (north anatolian fault): Implications for seismic hazard in istanbul. *Geochemistry, Geophysics, Geosystems*, *6*, 6009. doi: 10.1029/2004GC000896

Aslan, G., Lasserre, C., Cakir, Z., Ergintav, S., Özarpaci, S., Dogan, U., … Renard, F. (2019, 2). Shallow creep along the 1999 izmit earthquake rupture (turkey) from gps and high temporal resolution interferometric synthetic aperture radar data (2011–2017). *Journal of Geophysical Research: Solid Earth*, *124*, 2218-2236. Retrieved from `https://onlinelibrary.wiley.com/doi/abs/10.1029/2018JB017022` doi: 10.1029/2018JB017022

Bhattacharya, P., Rubin, A. M., Bayart, E., Savage, H. M., & Marone, C. (2015). Critical evaluation of state evolution laws in rate and state friction: Fitting large velocity steps in simulated fault gouge with time-, slip-, and stressdependent constitutive laws. *Journal of Geophysical Research: Solid Earth*, *120*(9), 6365–6385. doi: 10.1002/2015JB012437

Bohnhoff, M., Bulut, F., Dresen, G., Malin, P. E., Eken, T., & Aktar, M. (2013, jun). An earthquake gap south of Istanbul. *Nature Communications 2013 4:1*, *4*(1), 1–6. Retrieved from `https://www.nature.com/articles/ncomms2999` doi: 10.1038/ncomms2999

Bouchon, M., Karabulut, H., Aktar, M., Özalaybey, S., Schmittbuhl, J., Bouin, M.-P., & Marsan, D. (2021). The nucleation of the Izmit and Düzce earthquakes: some mechanical logic on where and how ruptures began. *Geophysical Journal International*, *225*(3), 1510–1517. doi: 10.1093/gji/ggab040

Bulut, F., & Doğru, A. (2021). Time frame for future large earthquakes near İstanbul based on east-to-west decelerating failure of the north anatolian fault. *Turkish Journal of Earth Sciences*, *30*(2), 204–214. doi: 10.3906/yer-2006-7

Cakir, Z., Ergintav, S., Akoğlu, A. M., Çakmak, R., Tatar, O., & Meghraoui, M. (2014, 10). Insar velocity field across the north anatolian fault (eastern turkey): Implications for the loading and release of interseismic strain accumulation. *Journal of Geophysical Research: Solid Earth*, *119*, 7934-7943. Retrieved from `http://doi.wiley.com/10.1002/2014JB011360` doi: 10.1002/2014JB011360

Cattania, C. (2019, sep). Complex Earthquake Sequences On Simple Faults. *Geophysical Research Letters*, *46*(17-18), 10384–10393. doi: 10.1029/2019GL083628

Corbi, F., Funiciello, F., Brizzi, S., Lallemand, S., & Rosenau, M. (2017). Control of asperities size and spacing on seismic behavior of subduction megathrusts. *Geophysical Research Letters*, *44*, 8227-8235. doi: 10.1002/2017GL074182

Şengör, A. M., Tüysüz, O., Imren, C., Sakinç, M., Eyidoğan, H., Görür, N., ... Rangin, C. (2005). The north anatolian fault: A new look. *Annual Review of Earth and Planetary Sciences*, *33*, 37-112. doi: 10.1146/annurev.earth.32.101802.120415

Dieterich, J. H. (1979, 5). Modeling of rock friction 1. experimental results and constitutive equations. *Journal of Geophysical Research: Solid Earth*, *84*, 2161-2168. Retrieved from `http://doi.wiley.com/10.1029/JB084iB05p02161` doi: 10.1029/JB084iB05p02161

Dieterich, J. H. (1992). Earthquake nucleation on faults with rate-and state-dependent strength. *Tectonophysics*, *211*(1-4), 115–134. doi: 10.1016/0040-1951(92)90055-B

Dublanchet, P., Bernard, P., & Favreau, P. (2013). Interactions and triggering in a 3-d rate-and-state asperity model. *Journal of Geophysical Research: Solid Earth*, *118*, 2225-2245. Retrieved from `http://doi.wiley.com/10.1002/jgrb.50187` doi: 10.1002/jgrb.50187

Erickson, B. A., Jiang, J., Barall, M., Lapusta, N., Dunham, E. M., Harris, R., ... Wei, M. (2020). The community code verification exercise for simulating sequences of earthquakes and aseismic slip (seas). *Seismological Research Letters*, *91*, 874-890. doi: 10.1785/0220190248

Fraser, J., Pigati, J. S., Hubert-Ferrari, A., Vanneste, K., Avsar, U., & Altinok, S. (2009, oct). A 3000-Year Record of Ground-Rupturing Earthquakes along the Central North Anatolian Fault near Lake Ladik, Turkey. *Bulletin of the Seismological Society of America*, *99*(5), 2681–2703. doi: 10.1785/0120080024

Gomberg, J., Beeler, N. M., Blanpied, M. L., & Bodin, P. (1998). Earthquake triggering by transient and static deformations. *Journal of Geophysical Research: Solid Earth*, *103*(10), 24411–24426. doi: 10.1029/98jb01125

Hairer, E., Wanner, G., & Nørsett, S. P. (1993). *Solving ordinary differential equations i* (Vol. 8). Springer Berlin Heidelberg. Retrieved from `http://link.springer.com/10.1007/978-3-540-78862-1` doi: 10.1007/978-3-540-78862-1

Herrendörfer, R., van Dinther, Y., Gerya, T., & Dalguer, L. A. (2015, 6). Earthquake supercycle in subduction zones controlled by the width of the seismogenic zone. *Nature Geoscience*, *8*, 471-474. Retrieved from `https://www.nature.com/articles/ngeo2427` doi: 10.1038/ngeo2427

Huang, Y., & Ampuero, J.-P. (2011, 12). Pulse-like ruptures induced by low-velocity fault zones. *Journal of Geophysical Research*, *116*, B12307. Retrieved from `http://doi.wiley.com/10.1029/2011JB008684` doi: 10.1029/2011JB008684

Kaneko, Y., Avouac, J.-P., & Lapusta, N. (2010). Towards inferring earthquake patterns from geodetic observations of interseismic coupling. *Nature Geoscience*, *3*, 363-369. Retrieved from `http://www.nature.com/articles/ngeo843` doi: 10.1038/ngeo843

Karabulut, H., Güvercin, S. E., Eskiköy, F., Konca, A. Ö., & Ergintav, S. (2021). The moderate size 2019 september m w 5.8 silivri earthquake unveils the complexity of the main marmara fault shear zone. *Geophysical Journal International*, *224*(1), 377–388.

Kato, N. (2004). Interaction of slip on asperities: Numerical simulation of seismic cycles on a two-dimensional planar fault with nonuniform frictional property. *Journal of Geophysical Research: Solid Earth*, *109*, 1-17. doi: 10.1029/2004JB003001

Kaya, T., Tank, S. B., Tunçer, M. K., Rokoityansky, I. I., Tolak, E., & Savchenko, T. (2009, 8). Asperity along the north anatolian fault imaged by magnetotellurics at düzce, turkey. *Earth, Planets and Space*, *61*, 871-884. Retrieved from `https://earth-planets-space.springeropen.com/articles/10.1186/BF03353198` doi: 10.1186/BF03353198/METRICS

King, G. C., Hubert-Ferrari, A., Nalbant, S. S., Meyer, B., Armijo, R., & Bowman, D. (2001, 11). Coulomb interactions and the 17 august 1999 izmit, turkey earthquake. *Comptes Rendus de l'Académie des Sciences - Series IIA - Earth and Planetary Science*, *333*, 557-569. Retrieved from `https://linkinghub.elsevier.com/retrieve/pii/S1251805001016767` doi: 10.1016/S1251-8050(01)01676-7

Koch, K.-R. (1999). Parameter estimation in linear models. In *Parameter estimation and hypothesis testing in linear models* (pp. 149–269). Springer.

Konca, A. O., Leprince, S., Avouac, J.-P., & Helmberger, D. V. (2010). Rupture process of the 1999 m w 7.1 duzce earthquake from joint analysis of spot, gps, insar, strong-motion, and teleseismic data: A supershear rupture with variable rupture velocity. *Bulletin of the Seismological Society of America*, *100*(1), 267–288.

Kondo, H., Özaksoy, V., & Yildirim, C. (2010, apr). Slip history of the 1944 Bolu-Gerede earthquake rupture along the North Anatolian fault system: Implications for recurrence behavior of multisegment earthquakes. *Journal of Geophysical Research: Solid Earth*, *115*(4), 4316. doi: 10.1029/2009JB006413

Lambert, V., & Lapusta, N. (2021, 10). Resolving simulated sequences of earthquakes and fault interactions: Implications for physics-based seismic hazard assessment. *Journal of Geophysical Research: Solid Earth*, *126*. Retrieved from `https://onlinelibrary.wiley.com/doi/10.1029/2021JB022193` doi: 10.1029/2021JB022193

Lambert, V., Lapusta, N., & Perry, S. (2021, mar). Propagation of large earthquakes as self-healing pulses or mild cracks. *Nature*, *591*(7849), 252–258. Retrieved from `http://www.nature.com/articles/s41586-021-03248-1` doi: 10.1038/s41586-021-03248-1

Lange, D., Kopp, H., Royer, J. Y., Henry, P., Çakir, Z., Petersen, F., … Géli, L. (2019). Interseismic strain build-up on the submarine North Anatolian Fault offshore Istanbul. *Nature Communications*, *10*(1). Retrieved from `http://dx.doi.org/10.1038/s41467-019-11016-z` doi:

10.1038/s41467-019-11016-z

Lapusta, N., Rice, J. R., Ben-Zion, Y., & Zheng, G. (2000). Elastodynamic analysis for slow tectonic loading with spontaneous rupture episodes on faults with rate- and state-dependent friction. *Journal of Geophysical Research: Solid Earth*, *105*(B10), 23765–23789. doi: 10.1029/2000jb900250

Lettis, C. A. H. E. A. A. B. J. B. W. (2003). Timing of late holocene earthquakes on the eastern düzce fault and implications for slip transfer between the southern and northern strands of the north anatolian fault system, bolu, turkey. *Turkish Journal of Earth Sciences*, *12*.

Liu, Z., & Wang, T. (2023, 8). High-resolution interseismic strain mapping from insar phase-gradient stacking: Application to the north anatolian fault with implications for the non-uniform strain distribution related to coseismic slip distribution. *Geophysical Research Letters*, *50*. Retrieved from `https://agupubs.onlinelibrary.wiley.com/doi/10.1029/2023GL104168` doi: 10.1029/2023GL104168

Lorenzo-Martín, F., Roth, F., & Wang, R. (2006, 10). Elastic and inelastic triggering of earthquakes in the north anatolian fault zone. *Tectonophysics*, *424*, 271-289. Retrieved from `https://linkinghub.elsevier.com/retrieve/pii/S0040195106002265` doi: 10.1016/j.tecto.2006.03.046

Luo, Y., & Ampuero, J. P. (2018). Stability of faults with heterogeneous friction properties and effective normal stress. *Tectonophysics*, *733*, 257-272. Retrieved from `https://doi.org/10.1016/j.tecto.2017.11.006` doi: 10.1016/j.tecto.2017.11.006

Nakatani, M. (2001). Conceptual and physical clarification of rate and state friction: Frictional sliding as a thermally activated rheology. *Journal of Geophysical Research: Solid Earth*, *106*(B7), 13347–13380. doi: 10.1029/2000jb900453

Nalbant, S. S., Bhloscaidh, M. N., Mccloskey, J., İpek, C., & Utkucu, M. (2023, 1). The role of stress barriers on the shape of future earthquakes in the mentawai section of the sunda megathrust. *Turkish Journal of Earth Sciences*, *32*, 320-329. Retrieved from `https://journals.tubitak.gov.tr/earth/vol32/iss3/7` doi: 10.55730/1300-0985.1847

Nie, S., & Barbot, S. (2022, 8). Rupture styles linked to recurrence patterns in seismic cycles with a compliant fault zone. *Earth and Planetary Science Letters*, *591*, 117593. doi: 10.1016/J.EPSL.2022.117593

Parsons, T. (2004). Recalculated probability of m$\geq$7 earthquakes beneath the sea of marmara, turkey. *Journal of Geophysical Research: Solid Earth*, *109*, 1-21. doi: 10.1029/2003JB002667

Perrin, G., Rice, J. R., & Zheng, G. (1995). Self-healing slip pulse on a frictional surface. *Journal of the Mechanics and Physics of Solids*, *43*(9), 1461–1495. doi: 10.1016/0022-5096(95)00036-I

Pondard, N., Armijo, R., King, G. C. P., Meyer, B., & Flerit, F. (2007, oct). Fault interactions in the Sea of Marmara pull-apart (North Anatolian Fault): earthquake clustering and propagating earthquake sequences. *Geophysical Journal International*, *171*(3), 1185–1197. doi: 10.1111/j.1365-246X.2007.03580.x

Pucci, S., Pantosti, D., Barachi, M., & Palyvos, N. (2007, 10). A complex seismogenic shear zone: The düzce segment of north anatolian fault (turkey). *Earth and Planetary Science Letters*, *262*, 185-203. Retrieved from `https://linkinghub.elsevier.com/retrieve/pii/S0012821X07004827` doi: 10.1016/j.epsl.2007.07.038

Rice, J. R. (1993). Spatio-temporal complexity of slip on a fault. *Journal of Geophysical Research: Solid Earth*, *98*(B6), 9885–9907.

Rosenau, M., Horenko, I., Corbi, F., Rudolf, M., Kornhuber, R., & Oncken, O. (2019). Synchronization of great subduction megathrust earthquakes: Insights from scale model analysis. *Journal of Geophysical Research: Solid Earth*, *124*, 3646-3661. doi: 10.1029/2018JB016597

Rubin, A. M., & Ampuero, J. P. (2005). Earthquake nucleation on (aging) rate and state faults. *Journal of Geophysical Research: Solid Earth*, *110*, 1-24. doi: 10.1029/2005JB003686

Ruina, A. (1983, 12). Slip instability and state variable friction laws. *Journal of Geophysical Research*, *88*, 10359-10370. Retrieved from `https://onlinelibrary.wiley.com/doi/full/10.1029/JB088iB12p10359` doi: 10.1029/JB088iB12p10359

Salditch, L., Stein, S., Neely, J., Spencer, B. D., Brooks, E. M., Agnon, A., & Liu, M. (2020, 1). Earthquake supercycles and long-term fault memory. *Tectonophysics*, *774*, 228289. Retrieved from `https://linkinghub.elsevier.com/retrieve/pii/S0040195119304044` doi: 10.1016/j.tecto.2019.228289

Schatzman, M., & Schatzman, M. (2002). *Numerical analysis: a mathematical introduction.* Oxford University Press on Demand.

Scholz, C. H. (2010). Large earthquake triggering, clustering, and the synchronization of faults. *Bulletin of the Seismological Society of America*, *100*, 901-909. Retrieved from `https://pubs.geoscienceworld.org/bssa/article/100/3/901-909/349641` doi: 10.1785/0120090309

Shi, P., Wei, M., & Barbot, S. (2022, 8). Contribution of viscoelastic stress to the synchronization of earthquake cycles on oceanic transform faults. *Journal of Geophysical Research: Solid Earth*, *127*. Retrieved from `https://agupubs.onlinelibrary.wiley.com/doi/10.1029/2022JB024069` doi: 10.1029/2022JB024069

Sopaci, E. (2022). *eyupsopaci/sbiem: intial release (version v.0.1.0)[software].* Zenodo. doi: 10.5281/zenodo.7419328

Sopaci, E., & Özacar, A. A. (2021, sep). Simulation of seismic triggering and failure time perturbations associated with the 30 October 2020 Samos earthquake (Mw 7.0). *TURKISH JOURNAL OF EARTH SCIENCES*, *30*(5), 653–664. Retrieved from `https://journals.tubitak.gov.tr/earth/vol30/iss5/7` doi: 10.3906/yer-2104-6

Sopacı, E. (2023). *Physics based earthquake triggering and fault interactions* (PhD thesis). Middle East Technical University.

Sopacı, E., & Özacar, A. A. (2023, 7). Impact of 2019 mw 5.8 marmara sea earthquake on the seismic cycle of locked north anatolian fault segment. *Tectonophysics*, *859*, 229888. Retrieved from `https://linkinghub.elsevier.com/retrieve/pii/S0040195123001865` doi: 10.1016/j.tecto.2023.229888

Stein, R. S., Barka, A. A., & Dieterich, J. H. (1997). Progressive failure on the north anatolian fault since 1939 by earthquake stress triggering. *Geophysical Journal International*, *128*(3), 594–604.

Thakur, P., & Huang, Y. (2021, 9). Influence of fault zone maturity on fully dynamic earthquake cycles. *Geophysical Research Letters*, *48*. Retrieved from `https://onlinelibrary.wiley.com/doi/10.1029/2021GL094679` doi: 10.1029/2021GL094679

Thomas, M. Y., Lapusta, N., Noda, H., & Avouac, J. P. (2014). Quasi-dynamic versus fully dynamic simulations of earthquakes and aseismic slip with and without enhanced coseismic weakening. *Journal of Geophysical Research: Solid Earth*, *119*, 1986-2004. doi: 10.1002/2013JB010615

Uçarkuş, G., Çakır, Z., & Armijo, R. (2011, 1). Western termination of the mw 7.4, 1999 İzmit earthquake rupture: Implications for the expected large earthquake in the sea of marmara. *Turkish Journal of Earth Sciences*, *20*. Retrieved from `https://journals.tubitak.gov.tr/earth/vol20/iss4/2` doi: 10.3906/yer-0911-72

Utkucu, M., Nalbant, S. S., McCloskey, J., Steacy, S., & Alptekin, Ö. (2003). Slip distribution and stress changes associated with the 1999 november 12, düzce (turkey) earthquake (mw= 7.1). *Geophysical Journal International*, *153*(1), 229–241.

Wei, M., Kaneko, Y., Shi, P., & Liu, Y. (2018, 5). Numerical modeling of dynamically triggered shallow slow slip events in new zealand by the 2016 mw 7.8 kaikoura earthquake. *Geophysical Research Letters*, *45*, 4764-4772. doi: 10.1029/2018GL077879

Wei, M., & Shi, P. (2021). Synchronization of earthquake cycles of adjacent segments on oceanic transform faults revealed by numerical simulation in the framework of rate-and-state friction. *Journal of Geophysical Research: Solid Earth*, *126*, 1-15. doi: 10.1029/2020JB020231

Wessel, P., Luis, J., Uieda, L., Scharroo, R., Wobbe, F., Smith, W. H., & Tian, D. (2019). The generic mapping tools version 6. *Geochemistry, Geophysics, Geosystems*, *20*(11), 5556–5564.

Yin, Y., Galvez, P., Heimisson, E. R., & Wiemer, S. (2023, 3). The role of three-dimensional fault interactions in creating complex seismic sequences. *Earth and Planetary Science Letters*, *606*, 118056. doi: 10.1016/J.EPSL.2023.118056

Yıkılmaz, M. B., Turcotte, D. L., Heien, E. M., Kellogg, L. H., & Rundle, J. B. (2015, 8). Critical jump distance for propagating earthquake ruptures across step-overs. *Pure and Applied Geophysics*, *172*, 2195-2201. doi: 10.1007/s00024-014-0786-y

Zabci, C., Akyüz, H. S., Karabacak, V., Sançar, T., Altunel, E., Gürsoy, H., & Tatar, O. (2011, jan). Palaeoearthquakes on the Kelkit Valley segment of the North Anatolian Fault, Turkey: Implications for the surface rupture of the historical 17 august 1668 Anatolian earthquake. *Turkish Journal of Earth Sciences*, *20*(4), 411–427. doi: 10.3906/yer-0910-48

Figure1.

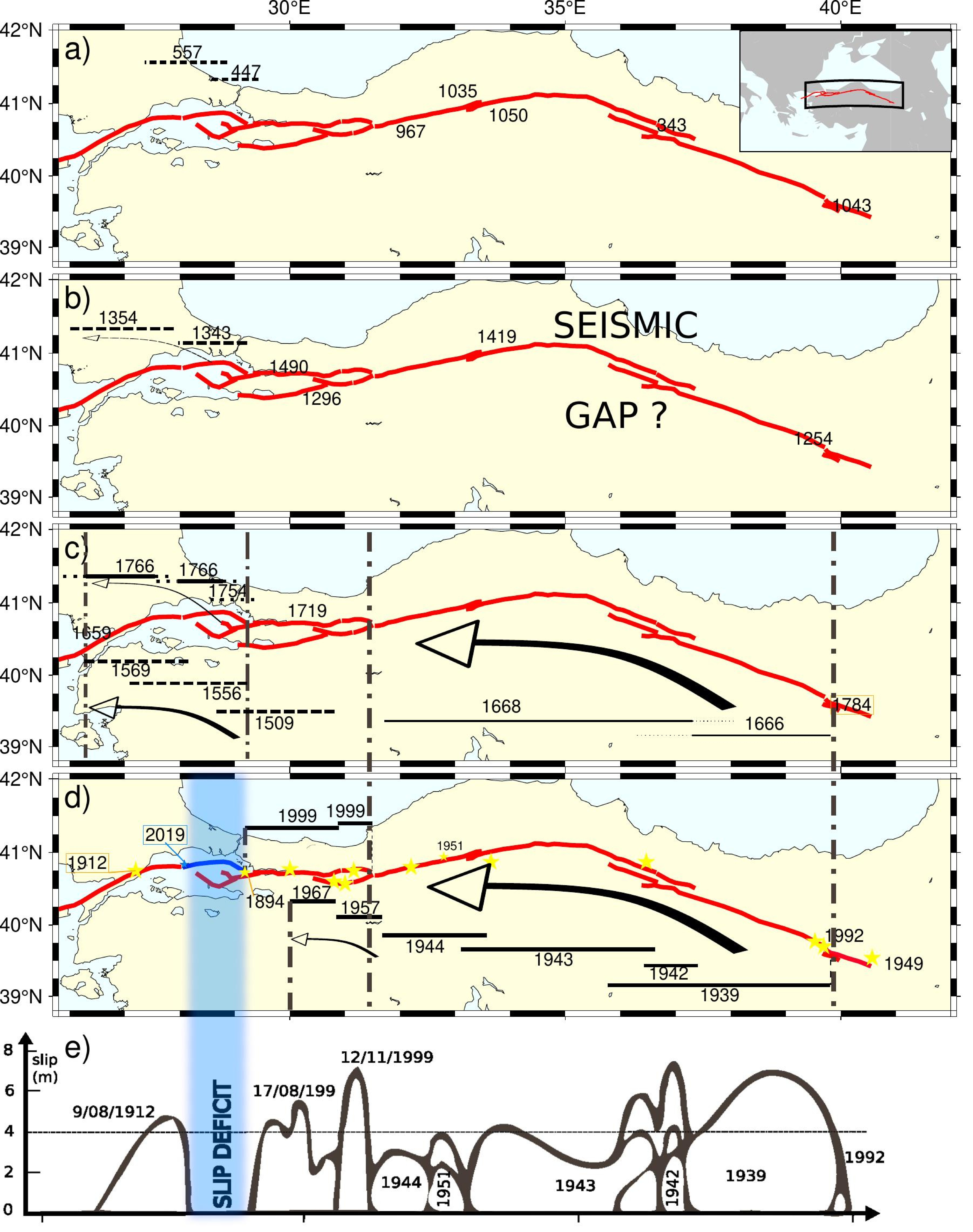
30°E
35°E
40°E
42°N
41°N
40°N
39°N
a)
557
447
1035
1050
967
343
1043
b)
1354
1343
1419
1490
1296
SEISMIC
GAP ?
1254
c)
1766
1766
1754
1719
1659
1569
1556
1509
1668
1666
1784
d)
1999
1999
2019
1912
1951
1894
1967
1957
1944
1943
1942
1939
1992
1949
e)
slip (m)
8
6
4
2
0
9/08/1912
17/08/199
12/11/1999
SLIP DEFICIT
1944
1951
1943
1942
1939
1992

Figure2.

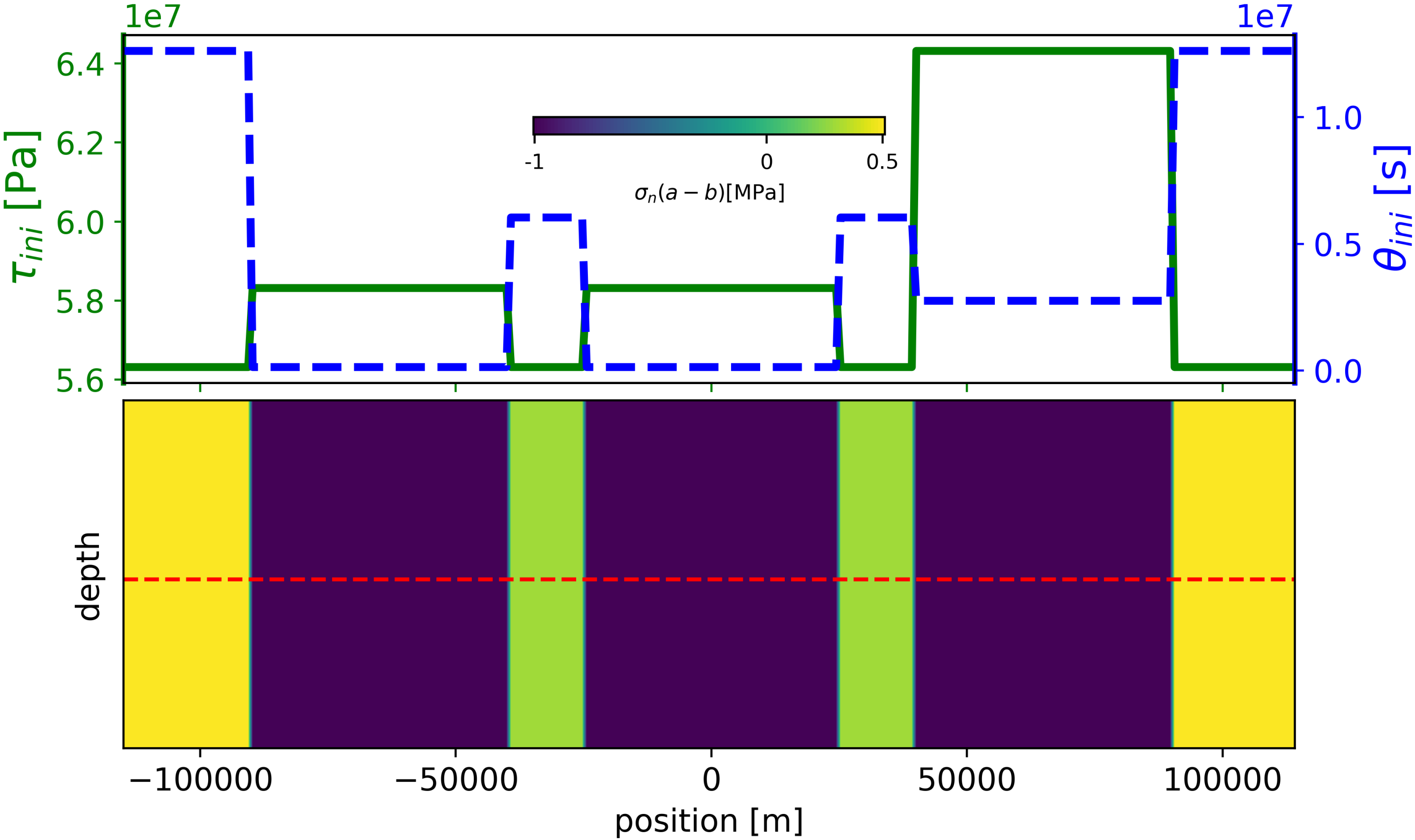
1e7
6.4
6.2
6.0
5.8
5.6
τ_{ini} [Pa]
1e7
1.0
0.5
0.0
θ_{ini} [s]
-1
0
0.5
$\sigma_n(a-b)$[MPa]
depth
−100000
−50000
0
50000
100000
position [m]

Figure3.

a)
slip [m]
35
30
25
20
15
10
5
position [m]
−100000
−50000
0
50000
100000
1
0
−1
−2
−3
−4
−5
−6
−7
−8
b)
left
middle
right
max
rate m/s
10^{-2}
10^{-6}
10^{-10}
Time [Year]
0
200
400
600
800
1000
1200
1400
c)
$\%\frac{|dt_f|}{\bar{T}}$
43.63
37.64
31.66
25.67
19.69
13.70
7.72
1.73
deviation
21.27
18.09
14.91
11.72
8.54
5.35
2.17
−1.01
middle-left
middle-right
conv.rate:-0.27
conv.rate:-0.15
cycle
2
4
6
8
10
12
14
16

Figure4.

a)
slip [m]
50
40
30
20
10
−100000
−50000
0
50000
100000
position [m]
1
0
−1
−2
−3
−4
−5
−6
−7
−8
b)
left
middle
right
max
rate m/s
10^{-2}
10^{-7}
10^{-12}
10^{-17}
0
500
1000
1500
2000
2500
Time [Year]
c)
$\%\frac{|dt_f|}{\bar{T}}$
24.49
20.83
17.18
13.52
9.86
6.21
2.55
−1.11
middle-left
conv.rate:-0.14
middle-right
conv.rate:-0.16
15.55
13.22
10.89
8.57
6.24
3.91
1.59
−0.74
deviation
2
4
6
8
10
12
cycle

Figure5.

a)
slip [m]
10
20
30
40
50
60
−100000
−75000
−50000
−25000
0
25000
50000
75000
100000
position [m]
1
0
−1
−2
−3
−4
−5
−6
−7
−8
b)
left
middle
right
max
rate m/s
10^{-2}
10^{-7}
10^{-12}
10^{-17}
0
500
1000
1500
2000
2500
3000
Time [Year]
c)
middle-left
conv.rate:-0.01
middle-right
conv.rate:-0.03
$\%\frac{|dt_f|}{\bar{T}}$
59.47
50.65
41.83
33.01
24.18
15.36
6.54
−2.28
deviation
23.75
20.39
17.04
13.69
10.33
6.98
3.63
0.27
2
4
6
8
10
12
14
16
cycle

Figure6.

a)
slip [m]
40
35
30
25
20
15
10
5
−100000
−50000
0
50000
100000
position [m]
1
0
−1
−2
−3
−4
−5
−6
−7
−8
b)
left
middle
right
max
rate m/s
10^{1}
10^{-2}
10^{-5}
10^{-8}
10^{-11}
0
250
500
750
1000
1250
1500
1750
Time [Year]
c)
middle-left
conv.rate:-0.16
middle-right
conv.rate:-0.25
83.8
68.3
52.8
37.3
21.7
6.2
−9.3
−24.8
103.7
88.1
72.6
57.1
41.6
26.1
10.6
−4.9
deviation
2.5
5.0
7.5
10.0
12.5
15.0
17.5
cycle

Figure7.

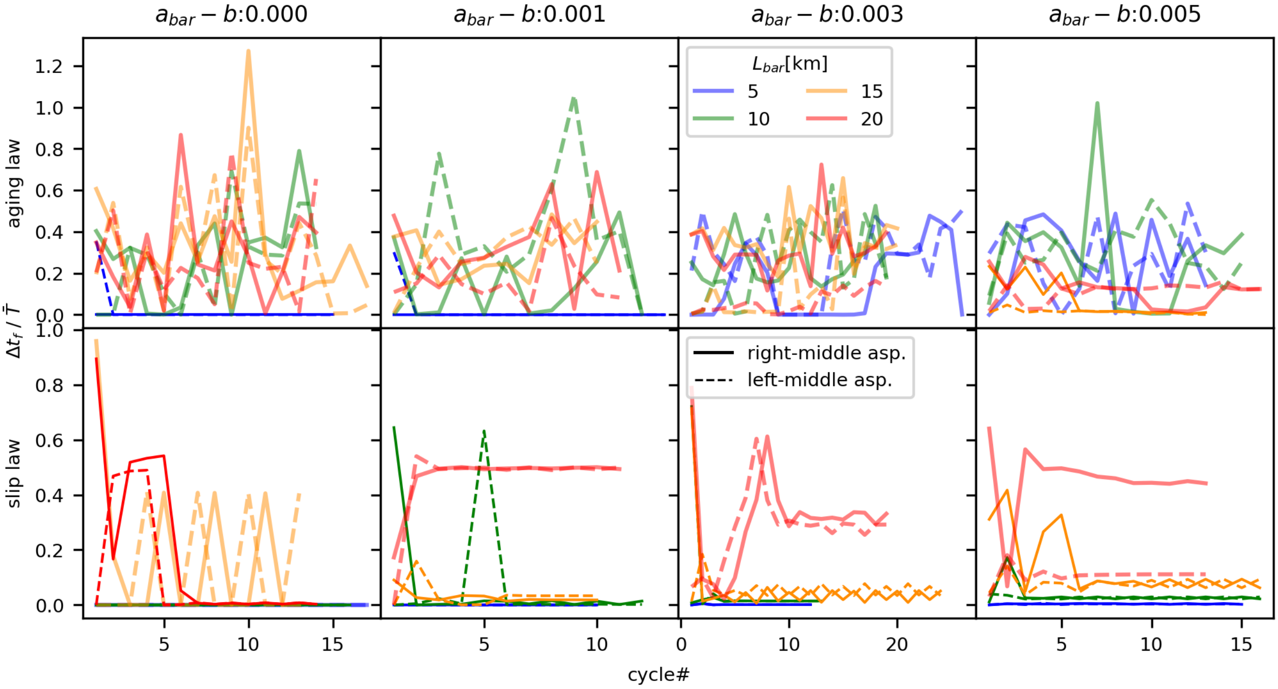
$a_{bar}-b$:0.000
$a_{bar}-b$:0.001
$a_{bar}-b$:0.003
$a_{bar}-b$:0.005
L_{bar}[km]
5
10
15
20
right-middle asp.
left-middle asp.
aging law
slip law
$\Delta t_f\ /\ \bar{T}$
0.0
0.2
0.4
0.6
0.8
1.0
1.2
0.0
0.2
0.4
0.6
0.8
1.0
5
10
15
0
10
20
cycle#

Figure8.

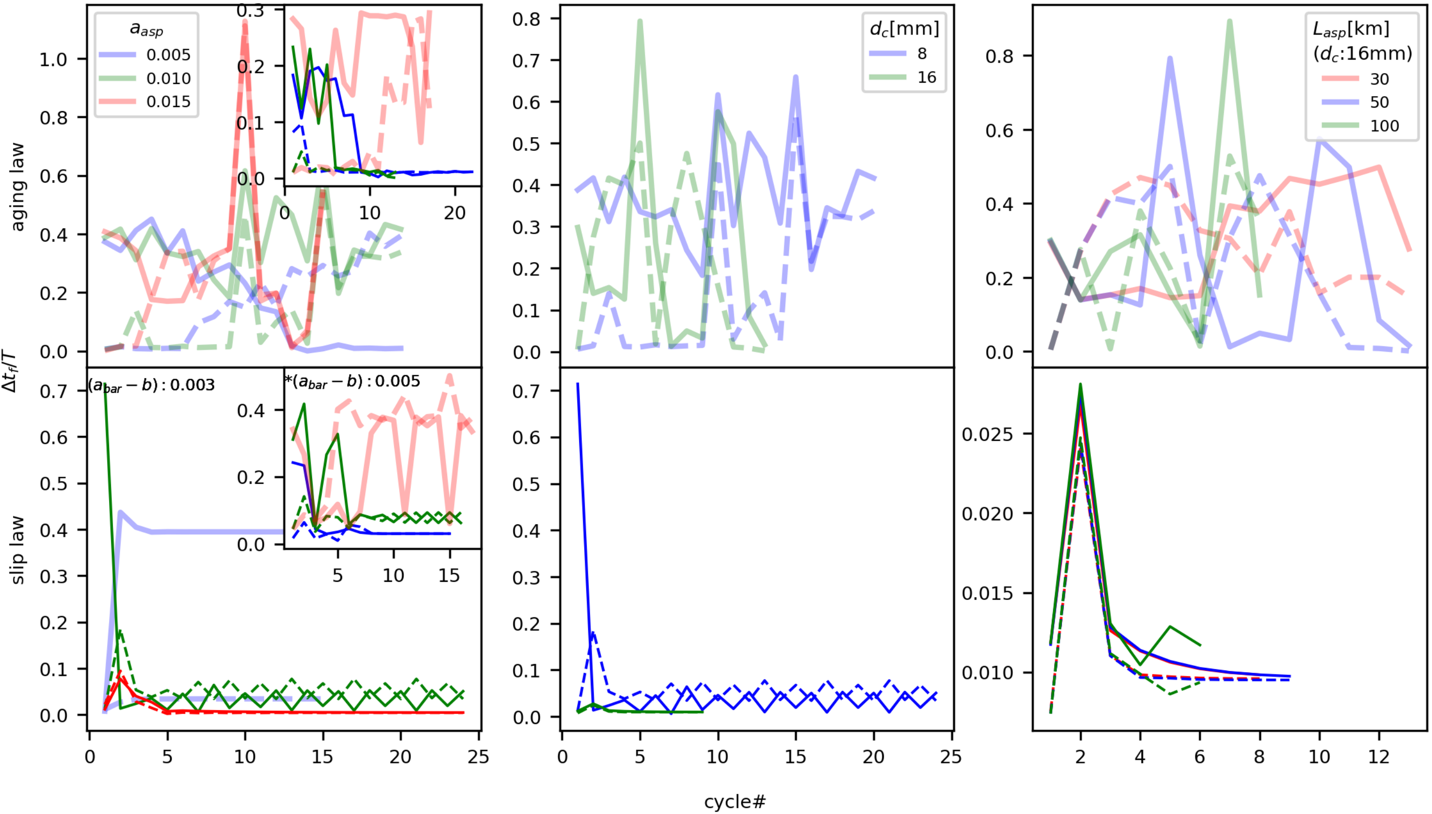
a_{asp}
0.005
0.010
0.015
d_c[mm]
8
16
L_{asp}[km]
(d_c:16mm)
30
50
100
aging law
slip law
$\Delta t_f/\bar{T}$
$(a_{bar} - b) : 0.003$
$*(a_{bar} - b) : 0.005$
cycle#
0.0
0.2
0.4
0.6
0.8
1.0
0.1
0.3
0.5
0.7
0.010
0.015
0.020
0.025
0
5
10
15
20
25
2
4
6
8
10
12

Figure9.

β_1
$\%\frac{|dt_f|}{\bar{T}}$
converged cycle
L_{bar} [km]
d_c [mm]
$a_{bar} - b$
a_{asp}
aging law
slip law
0.0
−0.2
−0.4
−0.6
−0.8
7.5
5.0
2.5
0.0
15
10
5
0
5
10
15
20
10
15
20
0.000
0.002
0.004
0.005
0.010
0.015

Figure10.

aging
min
hour
day
wk
mn
yr
2yr
slip
min
hour
day
wk
mn
yr
2yr
r.t:126.03yr
r.t:96.00yr
r.t:306.99yr
r.t:161.05yr
r.t:499.80yr
r.t:260.38yr
r.t:712.69yr
r.t:353.19yr
r.t:912.98yr
r.t:444.15yr
Shear stress [MPa]
Position [m]
−40000
−35000
−30000
−25000
−20000
0
20000
25000
30000
35000
40000
50
60
70
80
90
100

Figure11.

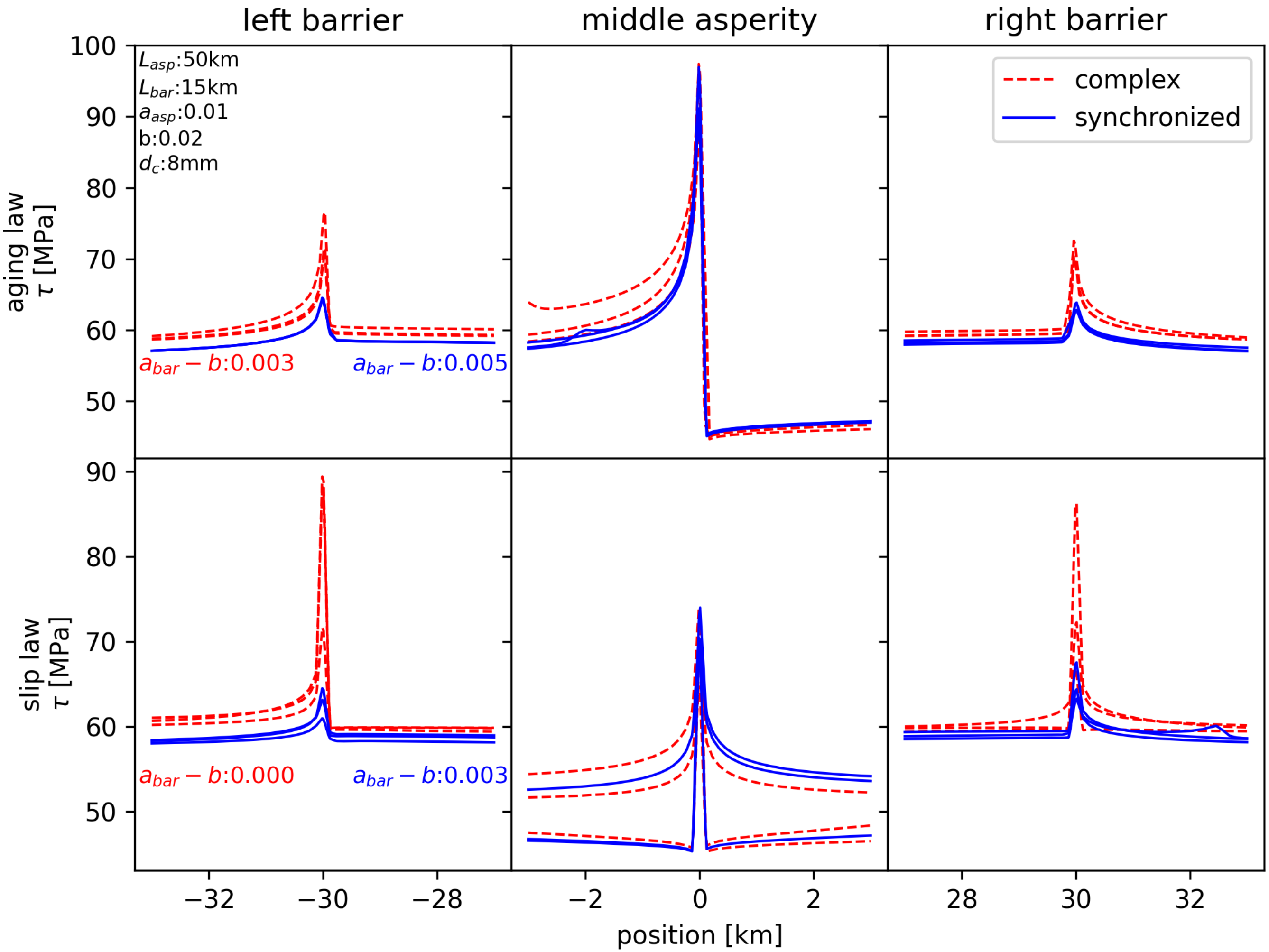
left barrier
middle asperity
right barrier
aging law
τ [MPa]
slip law
τ [MPa]
100
90
80
70
60
50
L_{asp}:50km
L_{bar}:15km
a_{asp}:0.01
b:0.02
d_c:8mm
$a_{bar} - b$:0.003
$a_{bar} - b$:0.005
complex
synchronized
90
80
70
60
50
$a_{bar} - b$:0.000
$a_{bar} - b$:0.003
−32
−30
−28
−2
0
2
28
30
32
position [km]

Figure12.

independent
complex
synchronized
□ aging
△ slip
rupture length[km]
10^2
post-seismic length[km]
10^2
10^1
pre-sesimic duration[day]
10^3
10^2
10^1
10^0
10^{-1}
post-seismic duration[day]
10^3
10^2
max wave speed Vs ratio[-]
10^0
mean stress drop[MPa]
10^1
6×10^0
4×10^0
3×10^0
Magnitude[Nm]
10^{19}
Partial ruptures ratio[-]
10^0
10^{-1}
uni-directional ruptures ratio[-]
10^0
6×10^{-1}
4×10^{-1}
3×10^{-1}
3×10^0
4×10^0
6×10^0
Peak slip rate [m/s]

Figure13.

a)
42.0°
41.0°
40.0°
39.0°
26.0°
28.0°
30.0°
32.0°
34.0°
36.0°
38.0°
40.0°
42.0°
Istanbul
Izmit
Düzce
Bolu
Ismetpasa
Gerede
Ezinepazari
Niksar
Erzincan
km
4
2
0
−2
b)
SLIP DEFICIT
2019
KB
30km
14km
CB
1999
KB : Kumburgaz basin
CB : Çınarcık basin
41.0°
40.5°
28.0°
28.5°
29.0°
29.5°
c)
Izmit
Düzce
~15km
Bolu
30.5°
31.0°
31.5°
d)
1942 Rupture
Niksar
Ezinepazari
10km
1939 Rupture
36.5°
37.0°
37.5°